Low–Temperature Chemical Vapor Deposition of Ruthenium and Manganese Nitride Thin Films

by

Teresa S. Lazarz

B.A., Knox College, 2004

DISSERTATION

Submitted in partial fulfillment of the requirements
for the degree of Doctor of Philosophy in Materials Science and Engineering
in the Graduate College of the
University of Illinois at Urbana–Champaign, 2009

Urbana, Illinois

Doctoral Committee:

Professor John R. Abelson, Chair
Professor Gregory S. Girolami
Professor Angus Rockett
Associate Professor Paul V. Braun
Associate Professor Susan K. Earles, Florida Institute of Technology

Abstract

Materials and thin film processing development has been and remains key to continuing to make ever smaller, or miniaturized, microelectronic devices. In order to continue miniaturization, conformal, low-temperature deposition of new electronic materials is needed. Two techniques capable of conformality have emerged: chemical vapor deposition (CVD) and atomic layer deposition (ALD). Here, two processes for deposition of materials which could be useful in microelectronics, but for which no low–temperature, conformal process has been established as commercializable, are presented. One is ruthenium, intended for use in interconnects and in dynamic random access memory electrodes, a known material for use in microelectronics but for which a more conformal, yet fast process than previously demonstrated is required. The other is manganese nitride, which could be used as active magnetic layers in devices or as a dopant in materials for spintronics, which is not yet established as a desired material in part due to the lack of any previously known CVD or ALD process for deposition.

A unique challenge arises in trying to grow impurity-free films of a catalyst. Ruthenium metal activates C–H and C–C bonds, which aids C–H and C–C bond scission. This creates a potential catalytic decomposition path for all metal–organic CVD precursors that is likely to lead to significant carbon incorporation.

Metallic ruthenium films can be grown by chemical vapor deposition from the organometallic precursor tricarbonyl(1,3–cyclohexadiene)ruthenium(0). This precursor is a highly volatile liquid, easy to synthesize and handle, and capable of delivering at least 0.26 Torr partial pressure at room temperature with-

out the use of a carrier gas. Because the precursor is a liquid, the vaporization rate is not subject to the problem of diminishing surface area that occurs with solid precursors. CVD proceeds readily for substrate temperatures $\geq$ 200 °C. The growth rates are high, up to 24 nm/min, which affords reasonable growth times of only a few minutes for film thicknesses of 50–100 nm. The catalytic activation of C–H and C–C bonds on ruthenium surfaces results in severe carbon contamination, around 30 atomic percent. The films are crystalline, and exhibit persistent $(0\,0\,0\,1)$ texture at low temperatures on all substrates used. The electrical resistivities of the films range from 24 to 219 $\mu\Omega\cdot$cm. The increase in resistivity above the bulk value of 7.1 $\mu\Omega\cdot$cm can be attributed to grain boundary scattering and the high carbon contamination levels. Films nucleate readily on covalent and oxide materials, in contrast to previously reported Ru precursors that require pretreatment of the substrate surface. The conformality of the films is excellent, even in trench structures with aspect ratios of 20 :1 .

Manganese nitride films were grown by chemical vapor deposition from the volatile manganese(II) amido precursor bis[di(*tert*)–butyl)amido]manganese(II) and ammonia. Between 80 and 200 °C, the films grown from bis[di(*tert*)–butyl)amido]manganese(II)contain crystalline η–Mn_3N_2. At 300 °C, a mixture of η- and ξ-phase manganese nitride with a manganese carbide impurity is deposited. Oxygen and carbon contamination in the bulk of the films is less than 1 atomic percent. Remarkably, the films are nearly completely crystalline at growth temperatures of 200 °C and above. The growth rate of 5.9 nm/min at 200 °C is also remarkably high for such a low growth temperature. The crystallinity and rapid growth rates are attributed to the labile metal–ligand bonding characteristic of high-spin Mn^{II}. As a result, reactive surface species remain mobile on the surface throughout much of the reaction pathway leading to nitride growth, and can settle into low-energy ordered arrangements before they become incorporated into the bulk by subsequent deposition activity.

Acknowledgements

This thesis would not have been possible without the support of many people.

Thanks go to my research advisor Dr. John R. Abelson for the salary, the equipment, and the advice on writing papers.

Thanks to my research co–advisor Dr. Gregory S. Girolami for improving my writing and the feedback on the chemistry aspects of my work.

Heartfelt thanks to Dr. Angus Rockett, who had the integrity and attention to not only recognize a severe problem when he saw it, but had the courage to do something about it.

Very heartfelt thanks to to Dr. Susan K. Earles, for both listening and being honest. I couldn't have asked for a better mentor.

Thanks to those who helped me with measurements: Subhash Gujrathi at the Université de Montreal for doing the TOF–ERDA measurements and calculations, and Dr. Bong–Sub Lee and Kristof Darmawikarta for taking the TEM images and diffraction patterns.

Thanks also to Drs. Mauro Sardela, Scott MacLaren, Rick Haasch, Nancy Finnegan, Tim Spila, Vania Petrova, and Doug Jeffers at the Center for Microanalysis of Materials for their extensive coaching, advice, availability and scientific input. Additional thanks to Mauro and Scott for the non–scientific discussions and the laughs.

Special thanks to Dr. Charles W. Spicer for making sure I had the supply of precursor I needed, the excellent teamwork at four in the morning, and the honeysuckle.

Without the wonderful staff and co-workers at Illinois Business Consulting, I would never have been introduced to project management. Thanks to Ron, Liezl, my managers, and my team members for providing me with the project management knowledge and experience to manage my thesis project instead of letting it manage me.

Thanks to all the wonderful women I met in the Society of Women Engineers, both old and young, who shared their experiences and triumphs so readily.

Thanks to all my friends, who were there for me when I needed them.

And finally, I thank my parents, Soile and Thomas Lazarz. Without their unwavering support and help, I would have left without a degree. Kiitos and tack.

Table of Contents

CHAPTER 1

Introduction

1.1 Introduction

1.1.1 Materials in the microelectronics revolution

Materials and thin film processing development has been and remains key to continuing to make ever smaller, or miniaturized, microelectronic devices. Miniaturization is also the aspect of the microelectronics revolution with the most immediate impact on technology, economics, and society.[1] Manufacturing integrated circuits by depositing and then shaping thin films (5–500 nm thick) one at a time into the electronic components required allows the best precision and miniaturization opportunities.[2] Because materials interactions[3–8] or process-dependent film properties[9, 10] can enable or disable adequate electrical functioning in the electric circuits, materials and processes have to be researched and selected in a coupled manner. Researching both new suitable materials and new thin film deposition processes that together give the right film properties for device manufacture enables integrated circuits and derivative technology to continue to move our global society in new directions.

The invention of the solid-state electronic device by John Bardeen, Walter Brattain, and William Shockley in 1947[11] to replace vacuum tube-based electronics started the microelectronics revolution. The invention of the planar integrated circuit by Noyce and Kilby in 1958[12, 13], together with the advantages of miniaturizing solid-state devices has lead to the creation of the $238 billion (2008)[14] semiconductor industry, which is still after four decades of growth projected to grow at a compound annual growth rate of 4.9% to $302

billion in 2013.[14] 84.4% of the global semiconductor market remains in integrated circuits.[14]

In addition to creating a new segment of manufacturing industry, integrated circuits have wider economic and societal impact. Together with fiberoptics, they have enabled the telecommunications revolution of global, instant communication and access to information, which in turn has been a significant driver of the global economy and globalization.[15, 16] The miniaturization and decreasing cost of integrated circuits has resulted in their incorporation into many devices that previously were analog, such as cars and refrigerators, but perhaps most strikingly has resulted in the spread of computers and computing to near saturation in the developed world[14]. Both globalization[15–19] and the spread of technology[18, 20, 21] have created such significant social change that very active efforts in existing and new academic fields are devoted to studying and understanding them.

Due to the requirement of materials compatibility, when miniaturization drives need for new materials for a component of an integrated circuit, two or more materials often need to be found which are mutually compatible and together give the required electrical properties. One example is the replacement of aluminum wires, or interconnects, with copper. The replacement required also finding a new material to prevent the copper from disabling the chips electrically by diffusing into nearby silicon and silicon dioxide[7, 22] as well as a copper–compatible material with a dielectric constant lower than that of silicon dioxide.[7, 8] Previously, interconnects were made from aluminum–copper alloys contained by titanium and titanium nitride films from the surrounding silicon dioxide.[7] The combination of these three materials worked well because the $Al-SiO_2$ interface is strong and dense[8] and the oxygen treatment that made the titanium nitride diffusion barriers perform well left oxygen to react with the aluminum to form a dense, confining layer of aluminum oxide.[7] As the interconnect lines became narrower and more closely spaced due to miniaturization, the resistive–capacitive coupling delay (RC delay) between adjacent lines increased until it became the major speed limiter.[7] In order to be able to continue miniaturization, a more conductive metal and an insulator with a lower dielectric constant to replace Al and SiO_2 were required.[7]

Although attempts were made to use TiN as a diffusion barrier for Cu, the

barriers that had performed so well together with Al failed to produce adequate materials and electrical performance.[7, 22] Without the oxygen treatment used previously, the TiN films allowed Cu atoms to diffuse through the barriers easily.[7, 22] However, due to the lack of a dense, diffusion–resistant copper oxide, the oxygen treatment of the titanium nitride that allowed them to function as diffusion barriers was not compatible with copper interconnects, and a new barrier material had to be found.[7, 22] Such couplings between materials, processing, and interfaces are common and may directly determine the usefulness of a particular material or film deposition process. Even the very heart of modern integrated circuits has required new materials to continue miniaturization. Hafnium–based high–permittivity dielectrics and metals are replacing silicon dioxide and polycrystalline, degenerately doped silicon in metal–oxide–semiconductor field effect transistors (MOSFETs),[23] which are the main logic element of integrated circuits. The hafnium–based high–permittivity dielectrics are only two of nearly 30 new materials in the 45 nm generation of integrated circuits that went into production in early 2007.[24]

Continuing to use familiar or similar materials is preferable. Straining silicon layers in MOSFETs has emerged as a widely used way to improve performance without new materials.[25] However, extending use of the same materials sets often requires new processes,[25, 26] which ideally should be extendable long beyond current needs. Miniaturization has driven three–dimensional stack– and trench–based production of dynamic random access memories (DRAMs), in order to accommodate increasing numbers of devices into the same surface area.[27] Three–dimensional DRAM production requires even coating of the three–dimensional features, meaning that even when using familiar materials, new deposition methods are necessary.[26, 27]

Due to the links between the materials, device design, circuit design, computer architecture, and software, a radically new device type may take 15 – 20 years to coordinate from the time a decision to make it is made.[28] The exit barriers become high once a technology has been committed to, and many avenues of research must be explored before it is feasible to make such a commitment. Microelectronics production and continued commercial innovation in the area depends on the creativity and exploration of countless research groups in creating new knowledge about designing and creating the different logic el-

ements of integrated circuits. In some instances, the time horizon is short and the goal clear, such as finding more conformal ways of creating the interconnects and metal contacts in integrated circuits.[29] Other times, the time horizon is long, and the basics of the idea implementation are still being researched, such as in spintronics. Spintronics is the idea to use electron spins, which are digital in the sense that they are only observed in one of two discrete states, as data bits instead of electric charges, as in electronics.[30] Both types of research are important and contribute to the future of micro– and nanoelectronics.

Semiconductor manufacture starts with a bare single–crystal silicon wafer. The wafer is doped with B and P atoms, oxidized to create SiO_2 to use as an insulator, then patterned and covered with films of other materials which are also patterned to build a layered structure that embodies the electrical circuits and devices. Later steps have to be done at low temperatures to avoid dopant diffusion away from their original locations in the silicon wafer, which ruins the devices. This need for low–temperature deposition processes is driving research into new starting molecules, or precursors, for thin film deposition that allow deposition materials at as low temperatures as possible.

1.2 Motivation

Miniaturization requires increasing aspect ratios, which requires even, or conformal, deposition into deep but narrowing holes. Interconnects are becoming deeper and deeper compared to their width, and are projected to become 2.9 times as deep as they are wide in 2022 compared to 2.3 in 2007.[29] While this may seem like a small change, no manufacturable solution for this was known in 2007. DRAM aspect ratios are also increasing, from 16 in 2007 to over 20 already in 2010. Especially in the case of DRAMs, coating these high–aspect ratio vias is a must for continued miniaturization.

The workhorse of electronic materials thin film deposition has traditionally been physical vapor deposition (PVD).[31] Physical vapor deposition techniques are based on evaporating or sputtering materials from a target onto a substrate. Because the common basis of the techniques is creating a flux of atoms toward the substrate, the sticking coefficient, or fractional probability

that the atom will stick to the surface, is very close to one as individual atoms are usually very reactive.[31] This means that films deposited using PVD cannot coat the insides of high aspect ratio features well.

Two techniques capable of conformality have emerged: chemical vapor deposition (CVD) and atomic layer deposition (ALD). Both techniques are based on delivery of a chemical compound (precursor) rather than atoms to the heated substrate. The precursor then reacts at the surface to form a material. Chemical vapor deposition is a continuous process, in which a precursor and often a co–reactant are injected into a vacuum chamber and react on the hot substrate surface. CVD precursors need to be sufficiently volatile to be delivered at least with the aid of a carrier gas flow into the vacuum chamber. Good CVD precursors are sufficiently stable to not decompose during handling, but unstable or labile enough to react at low deposition temperatures. Atomic layer deposition is performed in cycles of precursor and co–reactant exposure, separated by gas purges of the chamber. This results in very precise control of the film growth and makes ALD extremely conformal, but due to the slow growth per cycle and the time required for the cyclic growth ALD is also very slow.

Precursor development for ALD is also more complicated, especially for metals.[32] The precise control in ALD comes from selection of precursors and co-reactants that adsorb in a self–limiting way on the growth surface, so that the same (small) amount of precursor and co–reactant is left on the surface to react with the next pulse of reactant regardless of the fluxes and pressures in the deposition chamber. The precursor and the co–reactant must have a very aggressive reaction rate to achieve reasonable growth rates, and must also be sufficiently stable to avoid self–decomposition in addition to the basic volatility requirement of CVD.[33] Developing atomic layer deposition precursors that fulfill all of these requirements is very challenging. Chemical vapor deposition is faster than atomic layer deposition due to being continuous rather than pulsed, but is generally less pure and conformal than ALD. However, conformal deposition by CVD has been demonstrated when precursors do not react immediately upon reaching the substrate[34–36], and the larger flexibility in precursor design that CVD allows makes both CVD and ALD important techniques for conformal deposition of conformal films. This thesis will focus exclusively on chemical vapor deposition.

In order to continue miniaturization, conformal, low-temperature deposition of new electronic materials is needed. Due to the complexity of the task, interdisciplinary and synergistic work is needed to develop new CVD precursors, using both inorganic synthetic chemistry and engineering. (Figure 1.1) Designing and synthesizing CVD precursors that are volatile, stable enough for handling, yet reactive enough for low temperature deposition requires insight into both inorganic chemistry as well as synthetic chemistry. Operating a state–of–the–art vacuum chamber for chemical vapor deposition and gathering and interpreting information from the film properties requires engineering know–how and knowledge of thin film growth processes. The work described in this thesis is a result of a collaboration between the inorganic synthetic chemistry group of Prof. Girolami in the School of Chemical Sciences and the materials science engineering group of Prof. Abelson, both at the University of Illinois at Urbana–Champaign.

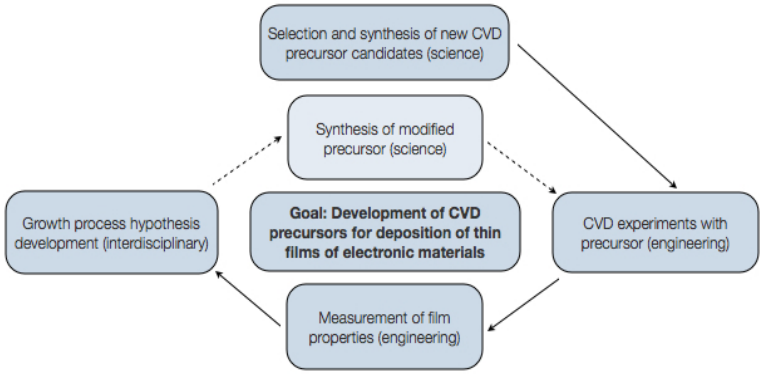

Figure 1.1: Scheme for chemical vapor deposition precursor development. Successful chemical vapor deposition process research and development requires interdisciplinary collaboration and knowledge.

Due to the coupling between materials and processes, a combination of basic science and engineering understanding of the thin film deposition processes is required in order to be able to contribute to the body of knowledge required for production decision–making. This thesis focuses on two examples of known materials which could be useful in microelectronics, but for which

no low–temperature, conformal process has been established as commercializable. One is ruthenium, intended for use in interconnects and in DRAM electrodes, a known material for use in microelectronics but for which a more conformal, yet fast process than previously demonstrated is required. The other is manganese nitride, which could be used as active magnetic layers in devices or as a dopant in materials for spintronics, which is not yet established as a desired material in part due to the lack of any previously known CVD or ALD process for deposition.

1.3 Organization

Chapter 2 outlines a new chemical vapor deposition process for ruthenium, based on the precursor tricarbonyl(1,3–cyclohexadiene)ruthenium(0), synthesized by Wontae Noh. The fundamentals of the deposition process are accounted for, such as growth rate, likely reaction equation, crystallinity, resistivity, and elemental composition.

Chapter 3 delves into the texture of the ruthenium films deposited by the process described in chapter 2. Due to the complexity of texture formation processes, the texture of the films is treated in a separate chapter. On all substrates, the ruthenium films exhibited clear overall texture at temperatures below 350 °C. The grain orientations form during film thickening, and are kinetically driven.

Chapter 4 describes the first chemical vapor deposition process for manganese nitride, based on the precursor bis[di(*tert*)–butyl)amido]manganese(II), developed and synthesized by Charles W. Spicer. Bis[di(*tert*)–butyl)amido]manganese(II) reacts with ammonia through a transamination reaction to form crystalline films at very low deposition temperatures, and specular, bronze–colored crystalline thin films can be deposited at temperatures as low as 80 °C.

Chapter 5 summarizes the findings of this thesis.

The contents of this dissertation is included in the following articles and presentations:

T. S. Lazarz, W. Noh, G. S. Girolami, and J. R. Abelson, *Low Temperature CVD of Ru from $C_6H_8Ru(CO)_3$*, Materials, Processes, Integration and Reliability in Advanced Interconnects for Micro- and Nanoelectronics, volume 990, edited by Lin, Q., Ryan, E. T., Wu, W. and Yoon, D. Y.

T. S. Spicer, C. W. Spicer, W. Noh, G. S. Girolami, and J. R. Abelson, *Chemical Vapor Deposition of Ruthenium Films from Tricarbonyl(1,3–cyclohexadiene)ruthenium(0)* Chem. Mat., submitted.

T. S. Spicer, C. W. Spicer, G. S. Girolami, and J. R. Abelson, *Texture in low-temperature chemical vapor deposited ruthenium films*, J. Cryst. Gr., to be submitted.

T. S. Spicer, C. W. Spicer, G. S. Girolami, and J. R. Abelson, *Low-Temperature Chemical Vapor Deposition of Manganese Nitride (η–Mn_3N_2) Thin Films from Bis[di(*tert*)–butyl)amido]manganese(II)and Ammonia*, Chem. Mat., to be submitted.

CHAPTER 2

Low–Temperature Chemical Vapor Deposition of Ruthenium Films

2.1 Introduction

Ruthenium is a noble, catalytic transition metal that until recently has mostly been of interest in heterogeneous catalysis. Relatively recently, ruthenium has been suggested as a material that could beneficially replace other metals and silicides in future generations of microelectronics components. Thin films of ruthenium may serve as electrodes in dynamic random access memories (DRAMs)[37–39] and ferroelectric random access memories (FRAMs)[40, 41], both of which are typically fabricated as high aspect ratio features. The electrical properties of ruthenium are similar to those of platinum, and Ru patterns easily with an oxygen plasma due to the volatility of ruthenium trioxide and tetroxide.[42–46]

Thin ruthenium films are also of interest as replacements for the metal gates in p–doped metal–oxide–semiconductor field effect transistors, also known as p–MOSFETs.[47] For p–MOSFETs, metal gate electrodes will be necessary to reduce the tunneling gate leakage current, especially when the gate dielectrics are high-k materials such as HfO_2, $HfSiO_x$, $HfNO_x$, and $HfSiNO_x$. The ~4.71 eV work function of Ru[48] is located almost exactly at the midpoint of the Si bandgap, so Ru is an attractive candidate as a single midgap gate material. The 4.2–4.3 and 5.04 eV work functions of Ru alloys and RuO_2, respectively[47, 49], also make these materials good candidates for dual metal gates.

An additional potential application of ruthenium films is as a combination adhesion promoter and electroplating seed layer between TaN and Cu in the copper dual damascene process.[50–54] Tantalum nitride, which is currently

used as a diffusion barrier for interconnects, cannot be electroplated directly with copper. In contrast, copper can be directly electroplated onto (and adheres well to) ruthenium.[55] By depositing a layer of ruthenium on the TaN barrier layer, copper adhesion would be improved and deposition of a copper seed layer would not be necessary.

2.2 Design of ruthenium chemical vapor deposition precursors

A unique challenge arises in trying to grow impurity-free films of a catalyst. Ruthenium metal activates C–H and C–C bonds, which aids C–H and C–C bond scission. This creates a potential catalytic decomposition path for all metal–organic CVD precursors that is likely to lead to significant carbon incorporation. Therefore, a key consideration in growing CVD films of catalytic metals such as ruthenium is combining molecule design and the kinetic aspects of growth in a favorable way. Ruthenium is a promising candidate for understanding chemical vapor deposition and precursor design of catalytic films.

Various chemical vapor deposition (CVD) precursors for ruthenium have been previously described, all in either oxidation state two or zero. Most have ruthenium in oxidation state two, requiring oxygen as a co–reactant to reduce the precursor metal center to metal. Most reported growth rates for pure ruthenium films are very low, presumably as a consequence of mitigating ligand decomposition by maintaining low precursor coverages. Ruthenocenes such as di(cyclopentadienyl)ruthenium(II)[56, 57] and bis(ethylcyclopentadienyl)ruthenium(II)[58–61] as well as ruthenium(II) β–diketonates[62–64] give pure films of low resistivity, but the growth rates are relatively slow. Much higher growth rates of 7.5 to 20 nm/min can be achieved on silicon and TiN substrates by using the precursor (cyclopentadienyl)(propylcyclopentadienyl)ruthenium(II). The films have low resistivities, but do not nucleate well on other substrates such as SiO_2, Si_3N_4, or air-exposed TiN.[65] Although the nucleation behavior on TiN can be improved by Ar plasma pre-treatment, this additional step is harsh and often incompatible with device fabrication process.

In addition to the ruthenium(II) precursors above, which must be reduced

to zero-valent Ru during CVD, several ruthenium(0) compounds have also been examined as CVD precursors. In theory, only metal-ligand bond breaking reactions are necessary to transform such precursors into metallic Ru films, because no redox chemistry is required. As a result, it may be possible to carry out depositions at lower temperatures. Triruthenium dodecacarbonyl ($Ru_3(CO)_{12}$) gives good-quality films, but the poor vapor pressure of this precursor complicates its practical use in a CVD process.[66, 67] The ruthenium arene complex (1,5–cyclooctadiene)(toluene)Ru(0) affords Ru films contaminated with carbon, owing to the activation of C–H bonds of the 1,5–COD ligand.[68] Under growth conditions that limit carbon incorporation to 1–3 atomic percent, the growth rates were $\sim$0.3 nm/min at best (by our analysis of their data). For the related compound (1,3–cyclohexadiene)(benzene)Ru(0), Ru films with as little as 3 atomic percent carbon could be obtained within a very narrow process window, but no growth rates were reported.[69, 70] The carbon incorporation was attributed to dehydrogenation of a fraction of the benzene molecules adsorbed on the surface. Deposition of Ru from an unspecified ruthenium(0) precursor has also been reported.[71] In summary, a precursor that affords pure ruthenium films at growth rates above 2 nm/min on a variety of substrates has yet to be found.

Surface science indicates a promising pathway for designing precursors that minimize the ligand decomposition. When benzene is adsorbed on a Ru surface, it does not fully decompose at low surface coverages.[72] If benzene and carbon monoxide are co–adsorbed on a ruthenium surface, the carbon monoxide acts like a spacer for the adsorbed benzene molecules[73], and the benzene saturation coverage goes down by a factor of two.[74] Furthermore, the presence of CO is known to suppress C–C bond scission reactions that lead to the decomposition of benzene on metal surfaces.[73] Carbon monoxide is known to desorb molecularly and essentially quantitatively from ruthenium surfaces at $\sim$275 °C in ultra–high vacuum.[75, 76] This strongly suggests that a Ru CVD precursor that results in CO and benzene molecules on the film surface could minimize ligand decomposition.

Tricarbonyl(1,3–cyclohexadiene)ruthenium(0), **1**, (figure 2.1) is a ruthenium CVD precursor with CO and 1,3–cyclohexadiene ligands. 1,3–cyclohexadiene and CO are both stable compounds, which has been theorized to minimize

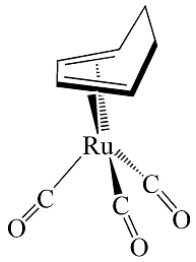

Figure 2.1: Structure of the chemical vapor deposition precursor tricarbonyl(1,3–cyclohexadiene)ruthenium(0), **1**.

ligand decomposition during Ru CVD.[68, 69, 77] Platinum, a chemically similar catalyst, catalyzes dehydrogenation of five– and six–member cyclic hydrocarbons into benzene.[78] The *d*–bands of ruthenium lie higher than those in platinum, generally predicting stronger ruthenium–adsorbate bonds than on platinum.[79] Although this has not previously been reported in the surface science literature, it is likely that ruthenium also catalyzes dehydrogenation of six–member hydrocarbon rings to benzene. This would result in the desired situation of benzene and CO co–adsorbed on the film surface.

Tricarbonyl(1,3–cyclohexadiene)ruthenium(0)is a pale yellow liquid that is thermally stable at room temperature and can be handled in air. The ligand–metal center bonds consist entirely of orbital overlap–type bonds, rather than electron exchange–type bonds, resulting in the ruthenium center being in oxidation state zero. The π orbitals of the 1,3–cyclohexadiene ligands overlap with the Ru *d* orbitals, as does the π^* orbital of the CO. The CO π^* orbitals often bond to metal centers in this way, called backbonding. Like other ruthenium(0) precursors, only ligand dissociation reactions are required to convert it to metallic ruthenium. The synthesis of **1**is facile, it is volatile, and it is stable for two weeks in air, making it an excellent precursor to work with.

In this chapter, the deposition of crystalline and conformal metallic ruthenium films from tricarbonyl(1,3–cyclohexadiene)ruthenium(0)is detailed. The results are discussed in light of previous precursor designs and challenges.

2.3 Experimental section

2.3.1 *Synthesis of tricarbonyl(1,3–cyclohexadiene)ruthenium(0),* ***1***

This precursor was synthesized by following a published procedure.[80, 81] No vacuum distillation was required. To prevent decomposition, the precursor was synthesized and stored under argon or in vacuum. Spectroscopic analysis yielded the following: ^{1}H NMR ($CDCl_3$): δ 5.48 (6 line 1:10:10:10:10:1 pattern; 4 most intense peaks give "J" = 5,3 Hz, inner CH), 3.26 (m, outer CH), 1.74 (dm, J_{gem} = 11 Hz, endo CH_2), 1.69 (dm, J_{gem} = 11 Hz, exo CH_2). $^{13}C\{^{1}H\}$ NMR ($CDCl_3$): δ 87.2 (inner CH), 55.5 (outer CH), 24.7 (CH_2). IR (neat): 3056 (w), 3005 (w), 2945 (w), 2927 (m), 2904 (m), 2876 (w), 2852 (m), 2057 (s), 1984 (s), 1468 (w), 1449 (w), 1435 (w), 1392 (w), 1328 (w), 1310 (w), 1255 (w), 1237 (w), 1182(w), 1138 (w), 1107 (w), 1072 (w), 1030 (w), 1000 (w), 940 (w), 874 (w), 859 (w), 845 (w), and 814 (w) cm^{-1}.

2.3.2 *Thermal characterization of* ***1***

Differential scanning calorimetry (DSC) studies were performed on a Mettler-Toledo DSC 821e, calibrated by octane, indium, and zinc standards. The heating rate was 10 °C/min. Each sample (∼6 mg) was accurately weighed (± 0.02 mg) into an aluminum pan, which was hermetically sealed. Standard open-container thermal gravimetric analysis (TGA) was performed in a Thermo Fischer Thermax 500 with a heating rate of 10 °C/min and a nitrogen flow rate of 350 cc/min. Isothermal TGA curves were also collected.

2.3.3 *Chemical vapor deposition (CVD) studies*

The films were deposited in a previously described chamber[36] of ultra–high vacuum construction with a base pressure of $5 \cdot 10^{-9}$ Torr at a precursor partial pressure of 0.030 mTorr, except for the macro–trench experiments, which were performed at 0.50 mTorr, as noted. However, the precursor was delivered through a tube of 3.8 mm inside diameter pointed directly at the substrate. Due to gas expansion effects into vacuum, the local flux is considerably larger than the average pressure of the chamber. Quadrupole mass spectrom-

etry of the gases in the chamber before film growth indicates that the majority of the background is dihydrogen, which is inefficiently pumped by the turbopump. Selected growths were monitored in-situ by quadrupole mass spectrometry (Balzers). Deposition temperatures were measured using a k–type thermocouple for all substrates except silicon, for which an infrared pyrometer (Omega) was used. Substrates were heated to 400 °C by radiative heating. Above 400 °C, silicon substrates were heated directly by Joule heating. Insulating substrates were clamped over a Joule-heated silicon backing plate. The temperature inhomogeneity due to contact differences when using resistive heating is estimated to be ± 10 °C. The precursor was kept at ambient temperature, and was delivered without a carrier gas from the stainless steel reservoir to the substrate. Growth was monitored with an in-situ ellipsometer (J.A. Woollam Co.). Deposition byproducts were analyzed with a downstream electron-impact quadrupole mass spectrometer (Balzers).

Ruthenium films were grown on degenerately doped n-type Si(1 0 0) (SiliconQuest International), wet thermally grown SiO_2, $Al_2O_3(0\,0\,0\,1)$ (Monocrystal), Corning 7059 barium–aluminum borosilicate glass (Corning), and cleaved KBr. For conformal coverage experiments, Si substrates were coated with 200 nm of Cr by thermal evaporation. Immediately before use, all substrates except KBr were cleaned ultrasonically by successive immersion in trichloroethane, acetone, isopropanol, and deionized (DI) water. Silicon substrates were rinsed in 10% HF solution to remove the native oxide, then flashed in vacuum to 600 °C in order to dehydrogenate the surface. The KBr substrate was cleaved from a larger crystal and had unknown surface roughness.

2.3.4 Ex-situ study of deposition byproducts

In order to determine the identities of the reaction byproducts, a film was grown in a previously described apparatus[82] (figure 2.2) that permits the volatile CVD byproducts to be condensed into an NMR tube and mixed with a deuterated solvent. The byproducts could be identified and their relative amounts quantified by ^{1}H NMR and ^{13}C NMR spectroscopy on a Varian Unity 500 instrument at 11.75 T. Chemical shifts are reported in δ units (positive shifts to high frequency) relative to TMS.

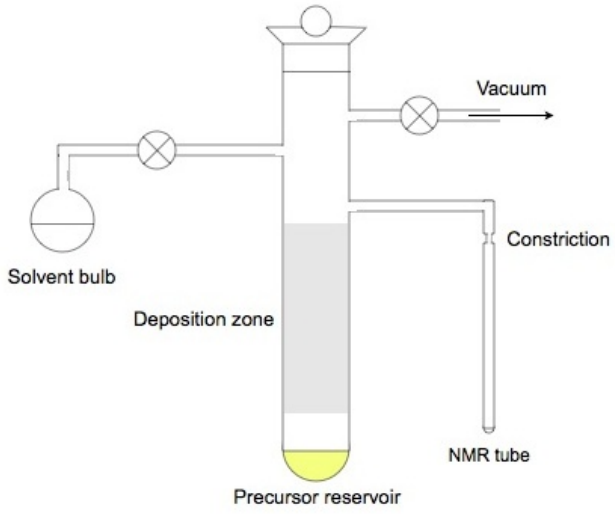

Figure 2.2: The glassware apparatus used for the trapping of the decomposition products of **1**.

2.3.5 Film characterization

Standard 2θ–ω X–ray diffraction (XRD) and glancing angle X–ray diffraction (GAXRD) patterns were collected on a Philips X'Pert 2 system using Cu Kα radiation. GAXRD at a constant glancing angle of 1° relative to the crystal planes most nearly parallel to the surface was performed in addition to standard 2θ–ω scans. Glancing angle measurements eliminate peaks due to the substrate because the X–ray beam enters the substrate only to a small extent, and also gives a greater signal to noise ratio because the beam interacts with a larger volume of film.

Fracture cross–sectional high resolution scanning electron microscopy (SEM) micrographs were obtained on a Hitachi S–4700 scanning electron microscope. To avoid charging effects on insulating substrates, a film of PtAu was sputtered over the samples to ensure good contact with the SEM ground. Resistivities were measured using a four-point probe. Auger electron spectra (AES) were collected on a Physical Electronics PHI 660 scanning Auger microprobe. Time-

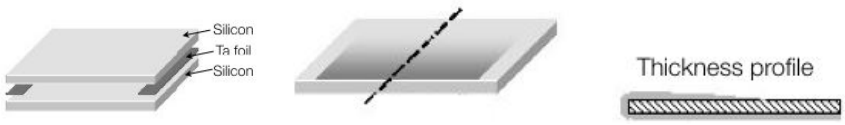

Figure 2.3: Construction and disassembly of a macrotrench. 2.3(a) shows the construction. 2.3(b) illustrates the cross–sectional cleavage of the Si macrotrench sides, which have some thickness profile (2.3(c)).

of-flight elastic recoil detection analysis (TOF–ERDA) elemental depth profiles were obtained using a 40 MeV Cu beam. To assess the nucleation density on SiO_2 substrates, films were grown only to the point of nucleation (as judged by in–situ spectroscopical ellipsometry) and then characterized with an Digital Instruments Dimension 3100 atomic force microscope, using a Nanoscope 3A controller in tapping mode. BudgetSensors TAP300A1 tips were used.

2.3.6 Conformality tests using a macrotrench

Ideally conformal films have the same thickness everywhere, even in recessed features such as trenches. If the precursor reacts too rapidly at the surface, deposition rates will be higher at the top of the opening than at the bottom, leading to the well-known pinch-off problem. If the reaction rate is rapid enough, the opening of the trench or via may close (or pinch off) altogether. A common metric for conformality is the trench coverage, defined as the minimum thickness at the bottom of the feature divided by the thickness at the top surface.

The conformality of the CVD Ru was measured in a macrotrench[35] consisting of two Cr-coated Si strips separated by 0.025 mm thick Ta foil spacers. (Figure 2.3.) The volume between the spacers is the macrotrench. The chromium coating on the sides assures that growth will proceed on all surfaces with essentially no nucleation delay, and that the film thickness is directly proportional to the steady-state growth rate. The precursor flow is directed in such a way that the inside of the macrotrench is not in the line of sight. The macrotrench was heated to 300 °C and the deposition carried out at a precursor partial pressure of 0.50 mTorr. After the deposition, the silicon plates were

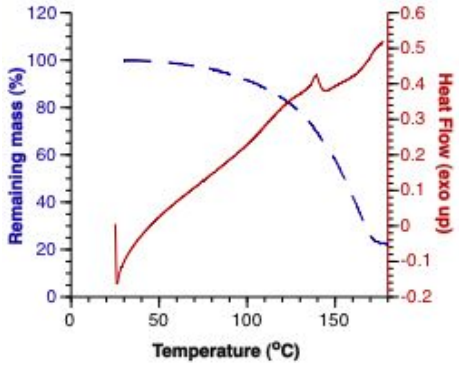

Figure 2.4: Thermogravimetric analysis (dashed line) and differential scanning calorimetry curve (solid line) of **1** at a heating rate of 10 °C/min.

separated, and the film thickness along the macrotrench measured by SEM to give information on conformality in a wide range of aspect ratios.

2.4 Results and discussion

*2.4.1 Thermogravimetric and differential scanning calorimetric analysis of **1***

TGA studies indicate that, under one atmosphere of N_2, **1** begins to lose mass at reasonable rates near 100 °C (figure 2.4), and very rapidly at 160 °C. Throughout this temperature range, DSC studies show that the heat flow is exothermic, presumably due to decomposition reactions that occur in parallel with evaporation. Upon completion of the TGA measurement, the sample container was coated with ruthenium both inside and outside. From isothermal TGA scans conducted below 160 °C, the mass decreases linearly with time, which indicates that mass loss follows apparent zero-order kinetics.

2.4.2 CVD reaction byproducts and reaction stoichiometry

The overall reaction responsible for CVD of ruthenium from this precursor is probably $(C_6H_8)Ru(CO)_3 \rightarrow Ru + C_6H_6 + H_2 + 3\,CO$. NMR analysis shows that

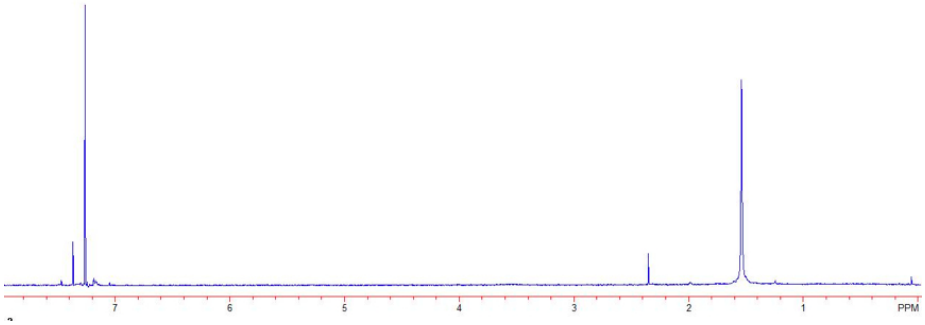

Figure 2.5: ^{1}H NMR spectrum of (incompletely) trapped reaction products in deuterated chloroform. The traces of water and toluene were present in the precursor batch before reaction. Water is a contaminant. Toluene was the synthesis solvent.

benzene is the only hydrocarbon formed when **1** is used to grow Ru films. No 1,3–cyclohexadiene could be detected. (Figure 2.5.) The in situ mass spectrum of the gaseous byproducts generated during ruthenium film growth show a very strong peak at m/e = 78 due to benzene, and only a weak signal at m/e = 80 due to 1,3–cyclohexadiene. Both results show that most of the 1,3–cyclohexadiene ligands are dehydrogenated to benzene on the film surface. The mass spectrum also shows that carbon monoxide is generated, and the amount formed is proportional to the amount of precursor consumed.

*2.4.3 Deposition of Ru films from **1***

Thin ruthenium films can be deposited from **1** by thermal CVD at temperatures ranging from 150 to 500 °C onto chromium, bare silicon, silicon dioxide, and *c*-plane sapphire substrates in the absence of a carrier gas. No nucleation occurs on hydrogenated silicon surfaces. The growth rates for deposition of Ru from **1** measured on chromium substrates ranged from 2 to 24 nm/min across this temperature range (Figure 2.6). Growth rates measured at selected tem-

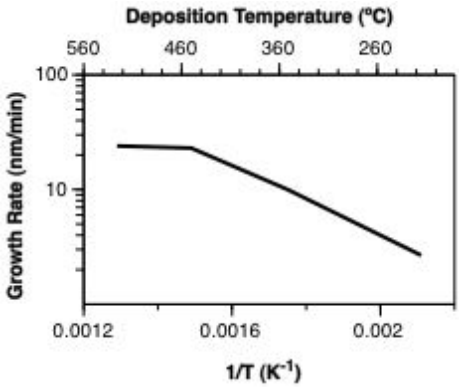

Figure 2.6: Arrhenius plot of growth rates vs temperature for ruthenium films grown via thermal chemical vapor deposition of **1**.

peratures on other substrates were similar. At a precursor partial pressure of 0.010 mTorr, the activation energy for deposition is 17 ± 7 kJ/mol. The process transitions from reaction-limited to flux-limited at 450 °C.

2.4.4 Crystallinity and grain size.

At all deposition temperatures (between 150 and 500 °C), the films are crystalline. (Figure 2.7.) All peaks in the GAXRD spectra of the films can be assigned to crystalline hexagonal Ru metal. Grain sizes extracted from Scherrer analyses are 20 – 24 nm at 200 and 300 °C, but increase to 60 – 210 nm at 400 and 500 °C. At deposition temperatures below 350°C, the films were $(0\,0\,0\,1)$ textured. The texture of the films will be discussed in chapter 3.

An attempt to quantify the stress in the films grown on sapphire was made. Standard XRD $\sin^2\psi$ methods are not applicable to textured films. Instead, a variant of the $\sin^2\psi$ method developed by Ma, Huang and Chen[83] was used. In the Chen group approach, the same x-ray geometry used in this study to obtain the GAXRD spectra was used and the sample tilted through a number of angles ψ. In order to improve signal to noise ratios, an X–ray lens was used. Spectra of the $(1\,1\,\overline{2}\,0)$ peak were collected. The lattice spacing d was determined for each angle ψ using center of gravity (CoG) peak fitting in the PC-STRESS program. For each sample, a plot of $\frac{d-d_0}{d_0}$ vs. $\cos\alpha \sin^2\psi$ was made,

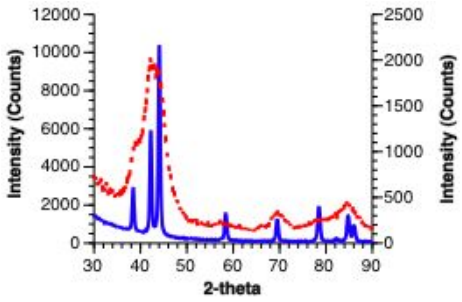

Figure 2.7: Overlay of glancing-angle x-ray diffraction patterns grown from **1** at 500 °C (red dashed line) and 200 °C (blue solid line). All peaks are due to hexagonal metallic ruthenium.

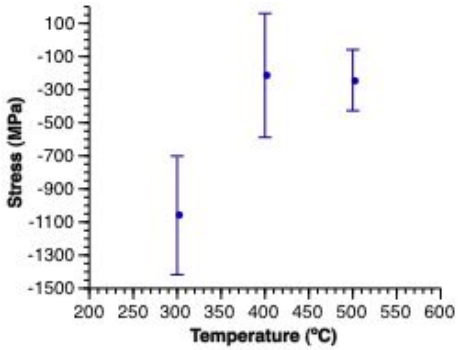

Figure 2.8: Calculated stresses in ruthenium films deposited from **1**, using a variant of the $\sin^2\psi$ method suitable for textured films.

where d is the measured lattice spacing at tilt angle ψ and d_0 the untilted lattice spacing. This is closely analogous to the standard $\sin^2\psi$ data treatment from tilting a Bragg-Brentano X–ray geometry, with only the factor of cos α accounting for the glancing angle in the geometry.

From the slope, the stress in the film can be calculated. The level of noise in the data from the film grown at the lowest temperature (200 °C) was too high to reliably calculate lattice spacings. As Ma, Huang and Chen do not suggest a new method for calculating errors in the stress, PC-STRESS was used to calculate the error in the stress as for standard $\sin^2\psi$ calculations. On sapphire,

the stress decreases with temperature. (See figure 2.8.) As there is a rotational honeycomb epitaxy possible for ruthenium on $Al_2O_3(0\,0\,0\,1)$[84], this may be due to increasing in-plane texture at higher temperatures, although there was not enough intensity to directly measure any in-plane texture with pole figures. It should be noted that even at 300 °C, these values are much lower than the values obtained for ruthenium films grown from RuCp(*i*-PrCp).[85]

2.4.5 Resistivity

For Ru films grown on insulating substrates, the room temperature resistivities decrease from ∼219 μΩ·cm to ∼24 μΩ·cm with increasing grain size (Figure 2.9). Bulk Ru has a resistivity of 7.1 μΩ·cm.[86] Resistivities could not be measured accurately on silicon substrates, because significant current passes through the substrate itself, but presumably the values are similar. The increase in resistivity above the bulk value can be attributed to grain boundary scattering and the high carbon contamination levels.

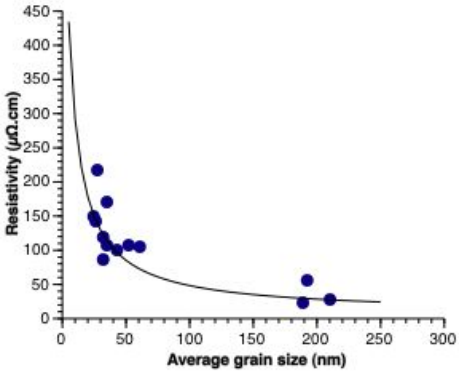

Figure 2.9: Measured resistivities of thin ruthenium films grown via thermal chemical vapor deposition from **1** (points), together with the resistivities predicted from the Mayadas-Schatzkes model for increases in resistivity due grain-boundary scattering as a function of grain size (line).

The resistivities of impurity-free thin films are generally larger than the bulk value due to three phenomena: electron–surface scattering, grain boundary scattering, and surface roughness–induced scattering.[87] Grain size effects

become important when the dimensions of the conductor approach two to three times the room temperature mean free path for electron-phonon collisions. When grain sizes are small, grain boundary scattering dominates in thin films[88], despite surface and interface scattering. Even when grain sizes are similar to total film thickness, grain boundary scattering is twice as important as surface scattering as a cause of resistivity increases.[89] To provide a qualitative check of size effects, we consider only grain boundary scattering using the model of Mayadas and Shatzkes, who represented grain boundaries as Dirac delta functions, the bottom and top surfaces as specularly scattering, and electron states as free–electron states.[90] Their model predicts that

$$\frac{\rho_0}{\rho} = 3[\frac{1}{3} - \frac{1}{2}\alpha + \alpha^2 ln(1 + \frac{1}{\alpha}], \tag{2.1}$$

where $\alpha = \frac{l_0}{d}\frac{R}{1-R}$, l_0 is the electron mean free path, d is the average grain size in the film, R is a parameter called the grain boundary scattering coefficient, ρ_0 is the bulk resistivity, and ρ is the measured resistivity. An R of zero corresponds to no scattering, while an R of one corresponds to complete scattering by a boundary. Despite the fact that the assumptions best describe main group metal films with columnar microstructures, the Mayadas–Schatzkes model has successfully been used to model other transition metal thin films.[91, 92] Although multidimensional models that account for tilted grain boundaries have been developed, the Mayadas–Schatzkes model does not deviate markedly from the multidimensional models over a large range of thicknesses. Because the Mayadas–Schatzkes model is simple and differs by around 7% at most from more complicated models[93], the Mayadas–Schatzkes model will give an excellent qualitative picture of size–related effects on film resistivities. Fitting the Mayadas–Schatzkes model to the resistivity and grain size data, using values of 10 nm for the electron mean free path and 7.2 $\mu\Omega\cdot$cm for the resistivity of bulk ruthenium at room temperature, affords an average grain boundary scattering coefficient of $\sim$0.98, indicating significant grain boundary scattering as expected. The prediction of the Mayadas–Shatzkes model using these parameters is shown in figure 2.9 as a solid line. The very high scattering coefficient required to achieve a good fit suggests that impurity scattering also appreciably raises the resistivity of the films, although impurity

scattering is not explicitly part of the model.

2.4.6 *Film purity*

The two main impurities of concern are oxygen and carbon. Detection of small amounts of carbon in ruthenium is problematic. Due to accidental overlaps between carbon and ruthenium peaks, and to the intrinsically lower sensitivity of carbon, neither AES nor X–ray photoelectron spectroscopy (XPS) can provide accurate measurements of the carbon content in a Ru film.[94, 95] By tracking the primary carbon peak at 273 eV and the secondary ruthenium peak at 231 eV in AES, an upper limit can be placed on the carbon content. For these films, this method gives upper limits of 1 – 7 atomic percent, but these estimates involve subtracting two large numbers, and are therefore not particularly accurate. TOF–ERDA is an absolute technique and was instead used to gauge the carbon impurity levels of four selected films.

In the interiors of the Ru films, the oxygen content of the films is below the detection limit (∼1 atomic percent) of AES. Using ERDA, the oxygen concentrations ranged between 1 and 3.8 at. %. However, the films were found to be severely carbon-contaminated, containing ∼30 at. % of carbon, along with trace amounts of hydrogen (Figure 2.10).

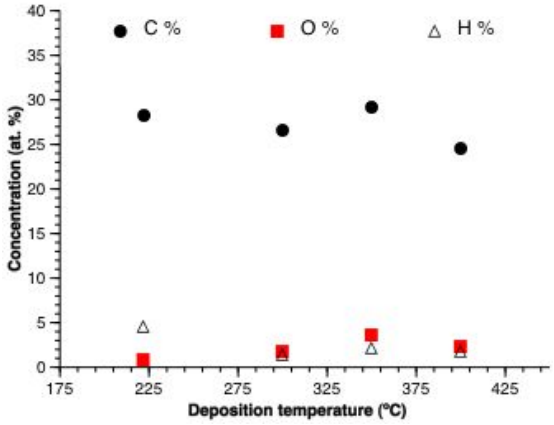

Figure 2.10: Carbon, oxygen and hydrogen impurities in four Ru films grown from **1** as measured by TOF–ERDA.

These results show that 1,3–cyclohexadiene and carbon monoxide ligands in **1** easily dissociate from the ruthenium center, but contrary to expectation react irreversibly on the Ru surface to a significant extent.

Benzene starts decomposing on ruthenium at 87 °C and dehydrogenates further on ruthenium surfaces into hydrocarbon fragments similar to those formed by acetylene and ethene on ruthenium surfaces.[73, 96] The decomposition of benzene into hydrocarbon fragments on Ru goes to completion at 277 °C[72], and CO desorbs molecularly from Ru at 275 °C.[75] Thus, it would be expected that carbon concentrations would be lower below 275 °C than above. This is not observed; rather, the carbon concentrations are similar across the range of growth temperatures. This indicates that neither previously theorized approach of lowering the benzene concentration on the surface compared to (1,3–CHD)Ru(benzene)[69] nor co–adsorption of benzene and CO[73] suppresses the activation of the C–H and C–C bonds of benzene on the surface sufficiently to avoid catalytic decomposition of the 1,3–cyclohexadiene ligand.

2.4.7 Nucleation delays and surface chemistry

Nucleation delays were measured in–situ by ellipsometry, which can detect the onset of growth at film thicknesses <1 nm. The delays were generally short, ranging between a few seconds to a few minutes, except on potassium bromide, on which films were very slow to nucleate. The lowest nucleation temperature was on silicon dioxide (170 °C), whereas the highest was on potassium bromide (350 °C). These differences in temperature windows and nucleation delays must be related to precursor–substrate surface interactions rather than the intrinsic decomposition rate of the precursor.

Figure 2.11 shows the ellipsometrically measured nucleation delays by substrate. There are two trends with increasing temperature. On silicon dioxide and sapphire substrates, nucleation delays approach zero as temperature increases. On silicon and Corning 7059 glass, nucleation delays first decrease and then increase again. The lowest nucleation temperatures were found on silicon dioxide, while the highest was found on potassium bromide. Because the decomposition temperature is 80 °C, these differences in temperature windows and nucleation delays are related to precursor–substrate surface chem-

istry and surface crystallography rather than the decomposition temperature of the precursor.

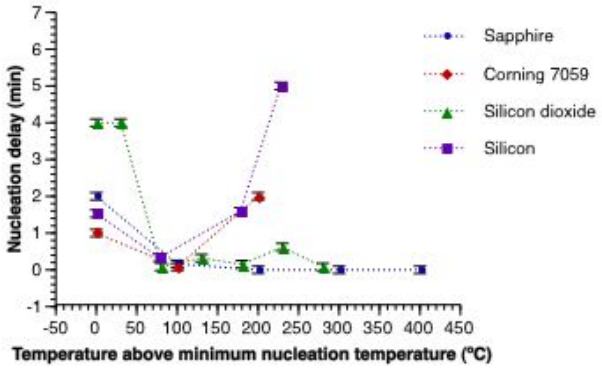

Figure 2.11: Nucleation delays of ruthenium thin films, shown as a function of temperature above the minimum required temperature for nucleation on each respective substrate.

Silicon substrates are initially hydrogenated, then feature localized dangling bonds and a non–epitaxial face–centered cubic crystal structure. Sapphire substrates are hexagonal epitaxial substrates and hydroxyl terminated. Silicon dioxide substrates are also hydroxyl terminated, but are amorphous. Corning 7059 substrates are also amorphous, but are a boron and barium-containing mixture of silicon dioxide and aluminum oxide. Potassium bromide is a salt with simple cubic crystal structure. From the lack of nucleation even after long exposures to precursor at temperatures where fairly rapid nucleation and growth on unhydrogenated silicon substrates occurs, it is clear that the precursor does not react with hydrogen to any significant degree. From the comparatively high first nucleation temperature on potassium bromide, the precursor also seems to react poorly with ions. From the extremely small nucleation delays on sapphire and low first nucleation temperature on silicon dioxide, it also seems clear that **1** interacts favorably with hydroxyl groups.

In order to create a qualitative picture of these precursor–surface interactions, the hard-soft acid-base principle (HSAB) offers simplicity and broad applicability. Although it cannot predict the outcome of every acid–base or redox reaction, it is easy to work with and deals with many in reality complicated

situations in a straightforward way that yields qualitative understanding. The key concepts from HSAB have been employed in density functional studies in surface science in order to understand chemisorption.[97] The effect of the solvent is also understood relative to molecules in the gas phase.[98] Therefore, applying HSAB to surface chemistry of CVD reactions ought be straightforward.

HSAB says that non–polarizable acids prefer to bind to non–polarizable bases and that polarizable acids prefer to bind to polarizable bases. Non–polarizable molecules are referred to as hard, whereas polarizable molecules are referred to as soft. Hardness and softness have been extended from typical acid–base reactions in water solution to encompass molecules of negligible proton basicity, including CO, aromatic hydrocarbons, unsaturated hydrocarbons, metals[98], and silicon surface states.[97] From the point of view of the HSAB principle, the π* backbonding between CO and Ru is a Lewis acid-base reaction between a soft acid (Ru) and a soft base (CO). Similarly, the π orbital overlap between 1,3–CHD and Ru *d* orbitals is a reaction between a soft acid and another soft base (1,3–CHD). Benzene is also considered a soft base.[98]

Bare silicon surface states are soft. The surface terminations of all other substrates used, including hydrogenated silicon, are hard. However, the terminating hydroxyl groups of the oxide surfaces are somewhat different from their solution counterparts in that they are bound to electropositive metals, which makes them acidic. (The hydrogen cation is extremely hard, having no electron cloud to polarize at all, and when bound to silicon lacks hydrogen binding possibilities.) The acidic hydrogen atom in the hydroxyl group can interact with the partial negative charge on the carbon monoxide oxygen atom, providing a chemisorption path for the precursor through hydrogen bonding. The nucleation on SiO_2 is indeed rapid and uniform, as detected by an AFM scan of a 32–second growth on SiO_2 at 300 °C (figure 2.12). Under these latter conditions, the nucleation density estimated from the AFM data is roughly 2300 nuclei/μm^2, and the root-mean-square (RMS) roughness is only 1.3 nm. The ellipsometric analysis shown in the inset to figure 2.12 reveals that nucleation is nearly instantaneous. The behavior at 200 °C is similar, but the roughness is slightly larger, 5.5 nm.

A completely different phenomenon may be behind the nucleation delay

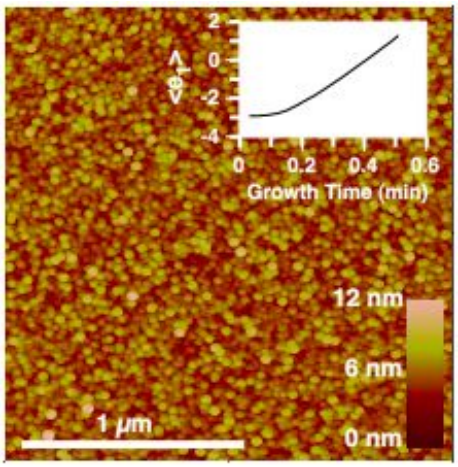

Figure 2.12: Atomic force microscope scan of a barely nucleated ruthenium film grown from **1** on SiO_2 at 300 °C. The root–mean–square roughness is 1.3 nm, and the nucleation density is $\sim$2300 nuclei/μm^2. Inset shows in–situ ellipsometric response during the 32–second growth.

on dehydrogenated silicon. Based on HSAB, it would be expected that because silicon surface states are soft and all parts of the precursor are soft, nucleation would be facile on silicon. This is not experimentally found to be the case. The reason for the chemical nucleation barrier lies in the high activity of silicon (similar to highly stepped platinum surfaces) for dehydrogenation of cyclic six-member hydrocarbons to benzene, releasing hydrogen as a byproduct.[99] The dehydrogenation proceeds readily already at 77 °C. However, in order to completely dehydrogenate a silicon surface, temperatures of over 600°C is required. At lower temperatures than this, some or all of the released hydrogen remains on the surface, blocking further nucleation since the precursor does not nucleate on hydrogenated silicon. Initial nucleation may be facile, but almost immediately blocks further nucleation. The nuclei must push aside the hydrogen, and growth rate differences determine when nuclei are large enough to be visible in ellipsometry.

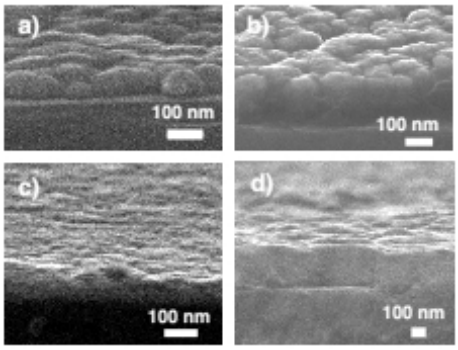

Figure 2.13: Microstructures of thin ruthenium films grown by thermal CVD from **1** on silicon substrates. Films grown at a) 220 °C, b) 300 °C, c) 400 °C, d) 450 °C.

2.4.8 Microstructure

There is significant variability in the microstructure of the Ru films, depending on substrate and temperature. On silicon, the films have a globular microstructure at low temperatures and flatten into compact, featureless microstructures at high temperatures (Figure 2.13). On Al_2O_3, an almost opposite trend is seen: at low temperatures, the films are compact and featureless and change abruptly above 350 °C to a bumpy morphology (Figure 2.14). On silicon dioxide and Corning 7059 glass, no significant change in microstructure is seen: on these substrates, the microstructures are compact and featureless at all temperatures.

These differences in microstructure may be due to the persisting effects of nucleation conditions on the films. The hydrogen bonding chemisorption path on silicon dioxide and glass is temperature–independent, accounting for the similar microstructures at all temperatures. On silicon, the hydrogen produced from the self-poisoning dehydrogenation of 1,3–cyclohexadiene remains on the surface at low temperatures, forcing the initial nucleation centers to grow granularly, pushing hydrogen out of the way, giving rise to the globular microstructure. As the temperature increases, a larger fraction of the hydrogen can leave the surface, giving rise to denser nucleation, which leads to smoother films, as observed. This is also supported by the microstructure of the film briefly nucleated at 450 °C and grown at 220 °C. This microstructure (figure 2.15) shows

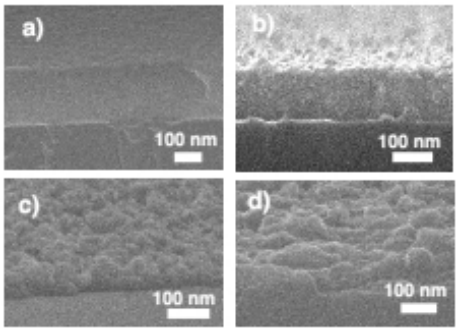

Figure 2.14: Microstructures of thin ruthenium films grown via thermal chemical vapor deposition from **1** on sapphire substrates. Films grown at a) 200 °C, b) 300 °C, c) 400 °C, d) 500 °C.

large thickness variations over large lateral length scales, suggesting sparse nucleation. The change in microstructure on sapphire substrates similarly suggests that the surface termination changes in a relevant way at higher temperatures. Oxygen depletion of the $Al_2O_3(0\,0\,0\,1)$ surface layer due to hydrogen exposure as well as thermal treatments have been observed.[100, 101] If the acidic hydroxyl groups were removed from the sapphire, the surface would be hard with no other clear interaction pathway between the precursor and the surface. Oxygen depletion due to thermal treatment has been observed at temperatures higher than the highest used here, 900 – 1400 °C.[100, 101] The initial facile nucleation followed by slower growth of a rough film with large grains may be due to the onset of a 'hardening' of the surface after initial nucleation, when a combination of moderate temperatures and hydrogen exposure could remove remaining hydroxyl groups. The films would then continue to grow mainly through grain growth, resulting in the microstructure observed.

2.4.9 Conformality

Conformality is the ability of a film to uniformly cover a deep feature such as a trench or a via (cylindrical well). It is of concern in microelectronic devices, which require the lining and filling of trenches and vias as key steps in the fabrication of memory cells and interconnects. The conformality of the film can be

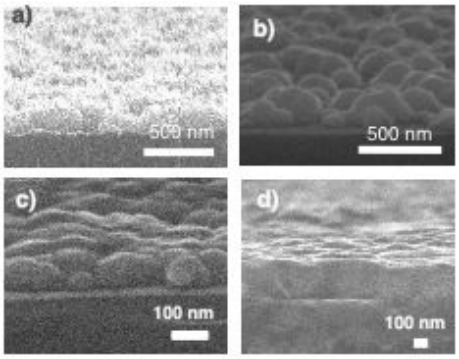

Figure 2.15: Microstructures of thin ruthenium films grown via thermal chemical vapor deposition from **1** on silicon substrates, nucleated at one temperature and growth optically opaque at another. a) Nucleated at 450°C and grown at 220°C b) Nucleated at 220°C and grown at 450°C. For comparison, c) shows the microstructure of a film grown on silicon at 220°C and d) shows a film on silicon at 450°C.

gauged by the ratio of the thickness of the film at a certain depth in the feature to the thickness of the film at the top of the feature. The conformality is often reported as a function of the normalized depth, which is the distance from the top of the feature divided by the width of the feature. For Ru films grown from **1** at 300 °C in a macrotrench (which has a near–infinite aspect ratio), the conformality is still a remarkable ∼90% at a normalized depth of 6, and has decreased only to ∼75% at a normalized depth of 20. In a via with aspect ratio of 20 : 1, the boundary condition imposed by the closed bottom is predicted to enhance the conformality to >90 %.[102] The conformality vs. normalized depth (Figure 2.16) has an unusual form, decreasing slowly to a depth of ∼30 and then quickly to zero.

This shape is consistent with numerical simulations of the rate of precursor consumption vs. local pressure in which surface site-blocking effects are present and lead to an enhancement in the conformality.[102] Therefore, tricarbonyl(1,3–cyclohexadiene)ruthenium(0) and its ligand set creates an inherently conformal growth process.

By solving the continuity equation in steady-state, a number of parameters can be calculated, including pressure inside the trench, growth rate and reac-

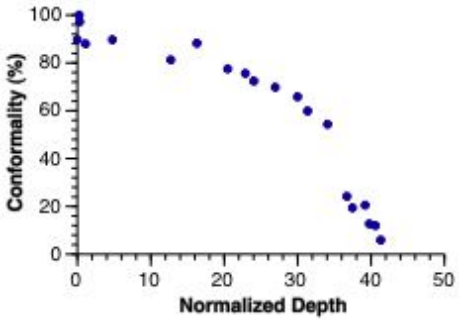

Figure 2.16: Conformality of Ru films grown from **1** at 300 °C with a precursor partial pressure of 0.50 mTorrinside a substrate macrotrench constructed out of chromium-covered silicon plates as a function of the normalized depth.

tion probability dependences on pressure.[102]

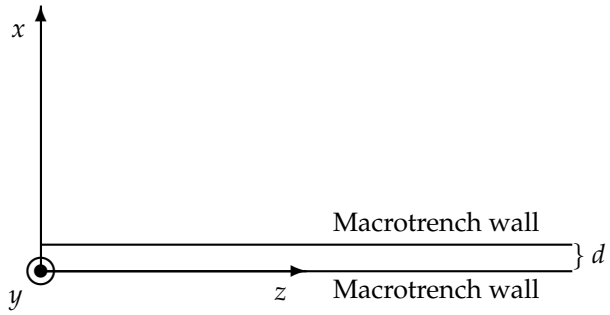

Figure 2.17: Coordinate system used in macrotrench analysis.

Consider a flux $\overrightarrow{J}$(x,y,z) entering a macrotench with plate spacing d, where J_z points into the macrotrench, J_y is in the direction of the open sides, and J_x is perpendicular to the walls. (Figure 2.17.) J_y will be lost out through the open sides of the macrotrench under the assumption of molecular flow. J_x has an unknown parabolic profile. However, $\overline{J_x}$ can be calculated, as will be shown below. In steady state,

$$\partial z J_z + \partial x J_x = 0, \tag{2.2}$$

subject to the boundary conditions

$$J_x|_0 = -r(z), J_x|_d = r(z), \tag{2.3}$$

where $r(z)$ is the growth rate as a function of position down the trench in $\frac{1}{m^{2 \cdot s^1}}$. To get the average flux profile, integrate equation (2.2) and divide by d:

$$\frac{1}{d}\int_0^d \partial_z J_z + \partial_x J_x \, dx = 0 \tag{2.4}$$

$$\frac{1}{d}\int_0^d \partial_z J_z dx + \frac{1}{d}\int_0^d \partial_x J_x \, dx \tag{2.5}$$

The first integral is

$$\int_0^d \partial_x J_x \, dx = J_x|_0^d = J_x(d) - J_x(0) = r - (-r) = 2r(z) \tag{2.6}$$

The second integral is

$$\int_0^d \partial_z J_z \, dx = \partial_z J_z x|_0^d = \partial_z J_z d \tag{2.7}$$

Substituting this in into equation (2.5), we obtain

$$\partial_z J_z + \frac{2}{d} r(z) = 0 \tag{2.8}$$

which gives us the change in flux down the trench in terms of the growth rate,

$$\partial_z \overrightarrow{J}(x, y, z) = -\frac{2}{d} r(z). \tag{2.9}$$

As d approaches infinity, $\partial_z J_z$ approaches zero. The physical meaning is that the relative importance of the wall losses depends on the spacing d, as would be expected.

The total material deposited past a point z is given by

$$\int_z^\infty -\frac{2}{d} r(z') \, dz' = J_z\infty - J_z(z). \tag{2.10}$$

In an open-ended trench, such as the macrotrench, $J_Z(\infty) \rightarrow 0$. That leaves

$$J_z(z) = \frac{2}{d}\int_z^\infty r(z')\,dz', \tag{2.11}$$

which describes the flux profile down the trench. (Figure 2.18)

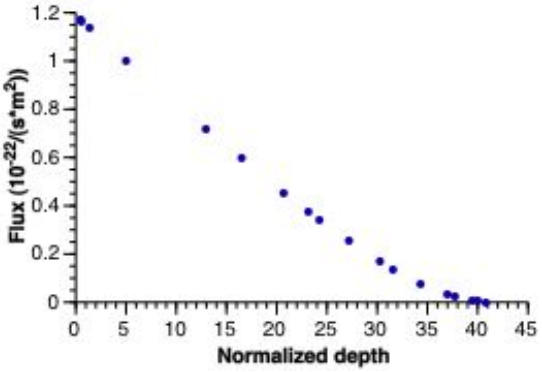

Figure 2.18: Profile of tricarbonyl(1,3–cyclohexadiene)ruthenium(0) flux down the macrotrench, calculated from equation 2.11.

Applying Fick's law, $J(x) = -D\frac{\partial\phi}{\partial x}$, to the flux profile yields

$$J_z(z) = -D\frac{\partial p}{\partial z}, \tag{2.12}$$

which can be easily solved for the pressure gradient along z and then integrated:

$$\frac{\partial p}{\partial z} = -\frac{J_z(z)}{D} \tag{2.13}$$

$$p(z) = \frac{1}{D}\int_z^\infty J_z(z)\,dz, \tag{2.14}$$

where D = $\frac{1}{3} < v_t > \kappa$. κ is an empirical constant on the order one, and was calculated based on the derivation Yang et al[102], which considers the conductivity of the trench, the mass of the molecule, and the relevant form factors. The pressure at the opening of the macrotrench is over 0.26 Torr, showing that tricarbonyl(1,3–cyclohexadiene)ruthenium(0) is capable of delivering a substantial partial pressure into a vacuum system. (Figure 2.19)

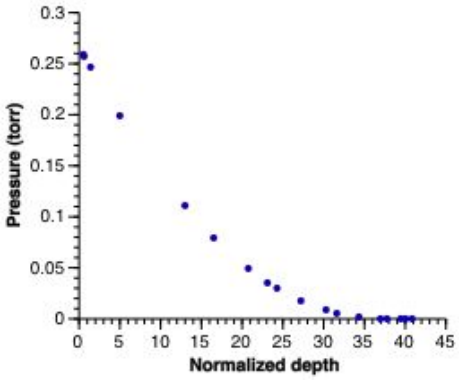

Figure 2.19: Profile of tricarbonyl(1,3–cyclohexadiene)ruthenium(0) pressure down the macrotrench, calculated from equation 2.14.

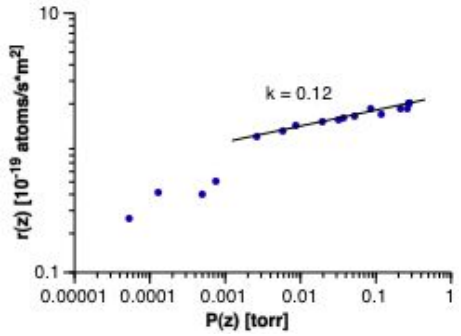

Figure 2.20: Relationship between growth rate and precursor pressure, calculated from equation 2.14.

Plotting the growth rate against the pressure shows that the growth rate is only weakly dependent on pressure (figure 2.20), with the growth rate growing as $p^{0.12}$ over a little more than two orders of magnitude. At pressures below 2 mTorr, the growth rate depends more strongly on pressure, suggesting that most ruthenium surface sites are blocked by ligands, reaction products, or the precursor itself at pressures above 2 mTorr.

Because the growth rate $r(z)$ has the units of flux, dividing the growth rate by the flux at each point z gives the reaction probability at each point z. (Figure 2.21.) The reaction probability of **1** is very low and shows a $p^{-0.46}$ dependence

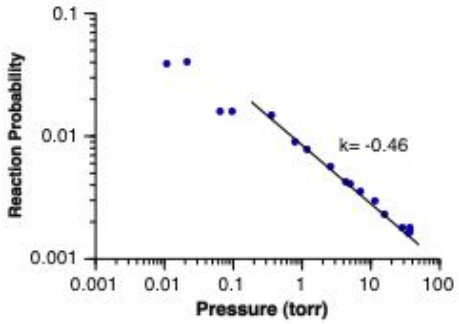

Figure 2.21: Reaction probability of a molecule of **1** at 300 °C as a function of the pressure.

on pressure over two orders of magnitude of pressure. This suggests that the siteblocking behavior is described at least roughly by a first–order Langmurian model, even though one would at first glance not expect the behavior to be linear over such a large pressure range based on a Langmurian model. However, if the siteblocking is due to reaction products rather than the precursor itself, the siteblocker pressure dependence of the reaction probability is unknown, as the partial pressure of reaction products is unknown.

CHAPTER 3

Texture in Chemical Vapor Deposited Ruthenium Films

3.1 Introduction

In a crystalline material, the texture which is the orientation of the grains relative to one another influences the properties of the material. In thin films used for microelectronics applications, the texture greatly influences the performance of the individual devices and ultimately the entire chip. A well-known example is the role of texture for electromigration resistance of interconnects.[103] When $(0\,0\,0\,1)$–oriented ruthenium films are used as an electroplating seed layer in the manufacture of copper interconnects, the deposited copper grains have a preference to align the $\{1\,1\,1\}$ crystal plane parallel to the $(0\,0\,0\,1)$ Ru surface plane.[52] This has been shown to improve the electromigration reliability of copper (Cu) interconnects[104], allowing the chips to function longer. Depositing the Cu films onto ruthenium films with the $(0\,0\,0\,1)$ crystal plane nearly parallel to the surface of the film has also been shown to lead to smoother morphologies and lower sheet resistances than depositing the Cu films onto other Ru crystal planes.[105] Also, controlling the crystal orientation of the underlying Ru has been suggested as an effective controlling parameter for achieving good Cu morphology.[105] Low–temperature texture formation in metal films is a phenomenon of both scientific and technological interest, as it is a result of a balance between kinetics and driving forces that affects the properties of the films, and thus affects the usefulness of the films for the intended applications.

In a textured film, grains prefer one or more crystallographic orientations compared to a random (“powder”) sample. Grain orientation parallel to the

surface of the film is called out of plane texture, where the plane is the plane of the film surface (and film–surface interface). (Figure 3.1.) Note, rotational orientation of the grains relative to the substrate crystal structure is called in–plane texture. Different ways of describing varying extents of texture include preferred orientation[106], fiber texture[106, 107], biaxial texture[108], and epitaxy. Preferred orientation refers to that there are more grains with specific crystal planes parallel to the surface compared to a powder sample.[106] Fiber texture in a film means all of the grains in the film are aligned with the same crystal plane facing up. However, the grains can be aligned differently rotationally with respect to the substrate.[106, 107] Biaxial texture means that all of the grains are aligned in the same way, and the grains are also aligned the same way rotationally with respect to the substrate crystal structure.[108] The grains may or may not have an epitaxial relationship to the substrate. In cases where biaxially textured film grains have an epitaxial relationship to the substrate, the biaxial texture is only different from epitaxy by the presence of multiple grains, rather than the single crystal of epitaxial growth. Although epitaxy is usually discussed as a phenomenon on its own, it is the limiting case of completely preferred orientation. The other types of texture can informally be thought of as 'partial epitaxy', in the sense that the grains of the film align in some way, but not as completely as in epitaxy. The other limiting case of texture is a completely random grain orientation, as in a powdered material where the grains have been randomized. In this chapter, the evolution of the texture in low-temperature chemical vapor deposited runthenium films will be presented.

Many attempts to explain texture formation in thin films have been made in the past 40 years.[109–117] Over time, an understanding has developed that texture formation is a sometimes complex interplay between driving forces[111, 112, 114, 115] and kinetics.[113, 118] It is also understood the outcomes vary for different materials, substrates, and deposition conditions. [117] This complexity necessitates theories that do not attempt to describe every detail of the texture creation process, but simplify in order to capture the main features.

In the first section, the general relationship between temperature and growth kinetics is discussed. Since texture has been shown to form during all stages of film growth [117] the texture formation during the following processes will be discussed: nucleation and pre-coalescence growth before coalescence of is-

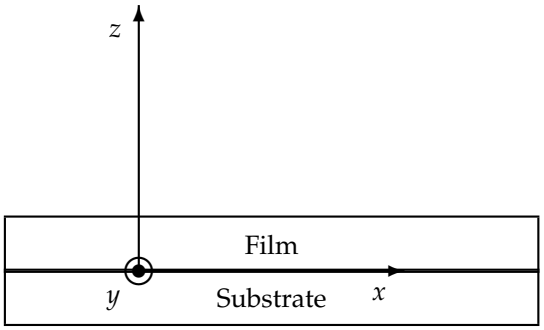

Figure 3.1: Illustration of reference coordinate system for texture orientation. Out of plane texture is texture in the z direction as indicated here; in–plane texture is relative to the x–y plane.

lands, formation during coalescence of islands, and evolution during thickening of the continuous film. Finally, the general evaluation of film growth kinetics is presented.

Despite the importance of texture in determining film properties and performance and such significant previous work in the area of understanding texture formation, few authors have measured the texture of ruthenium films. Strong $(0\,0\,0\,1)$ texture in ∼120 nm thick sputter–deposited ruthenium films has been investigated and attributed to energy minimization, based on the commonly accepted assumption that the close-packed basal plane $(0\,0\,0\,1)$ has the lowest surface energy.[119] However, modified embedded atomic method calculations have found the minimum surface energy plane for ruthenium to be $(1\,1\,\bar{2}\,0)$.[120] This apparent contradiction calls for closer examination. In sections 2 and 3 of this chapter, the texture of ruthenium films deposited from **1** is presented and analyzed.

3.1.1 Why thin films may exhibit texture

Driving forces, defined by thermodynamics, only determine the results of phenomena when sufficient energy is available to overcome kinetic barriers such as recrystallization energies and hopping barriers of surface diffusion, i. e. close to equilibrium conditions.[113, 118] Even very strong driving forces may not

directly determine process rates at all.[121] However, it can be shown that the substrate temperature in relation to the melting point of the material of the film, the homologous temperature T* = T/T_m, is the primary determiner of the kinetics of the film growth.[122]

At high T*, bulk chemistry and diffusion dominate and the driving forces are kinetically enabled to determine the outcome of both film microstructure and crystallographic texture.[122] Energy minimization as well as texture formation theories that require the availability of grain boundary mobility and high surface mobility are applicable at high homologous temperatures. At intermediate homologous temperatures, some but not all outcomes predicted by driving forces are kinetically possible.

At low T*, however, the film growth is severely kinetically limited due to low or nonexistent grain boundary and surface mobilities. At low homologous temperatures, the texture as well as the microstructure, is dependent on a number of different parameters.[122] Because both texture and microstructure depend on the same kinetic limitations, the film microstructures may lend clues to the degree of kinetic limitation in a particular system.[122] Considering the kinetic information that the microstructures of the films carry in conjunction with the measured crystallographic texture information aids in determining how texture could have formed. For materials with high melting points such as ruthenium, any low-temperature growth occurs at temperatures far below those at which adatom mobilites and grain boundary mobilities are significant. Even when the homologous temperature is low, relatively pure metals deposit into crystals.[113] However, they often lack texture.[116, 122]

3.1.2 Texture formation during nucleation and before coalescence of islands

Any periodicity in the substrate surface can be expected to be most important during nucleation. Crystalline substrates influence texture through initial local pseudomorphic epitaxy, even though the final structure of the film will not necessarily be epitaxial with the substrate.[116] Conditions for continuing epitaxy past the nucleation stage have been thoroughly been discussed elsewhere and are out of scope for the present work. Small nucleation barriers and

amorphous substrates have been experimentally found to lead to randomly oriented islands at low temperatures.[116] This suggests that high nucleation barriers and a crystalline substrate may contribute to texture formation during nucleation. Nucleation kinetics are affected by the adatom binding energy, crystal structure of the substrate material, lattice defects, surface steps, and contamination.[116] Due to being relatively easily observed, the first two have been explored in relation to texture formation. Surface steps have also been considered, using the assumption that high–energy planes have a higher step density than low–energy planes.

Considering the interactions between adatoms and the surface is central to one of the oldest theories of texture formation, Walton's preferred nucleation theory. The preferred nucleation theory is based on preferred orientations arising due to cluster–substrate alignment or, in the absence of strong substrate influence on orientation, due to the number of adatom–adatom bonds required to form a stable cluster on the substrate surface.[111] This model posits that texture is driven by the concept that most of the nuclei on a substrate ought to be those that have the lowest potential energy.

Walton argues that if the supersaturation of adatoms on the surface is high (i. e. low substrate temperature or high incidence rate), a single bond between an adatom and the substrate can act as a stable cluster. Unless the substrate causes orientation in the clusters as they grow, the process of grain growth will then be essentially random and no orientation will result. A low nucleation barrier would presumably aid in stabilizing a single adatom–substrate bond. Spacings between such grains at high supersaturations ought to be around 100 Å or less[117], while grain sizes so small are rarely observed. This suggests that coarsening or ripening has occurred in films with larger grain sizes nucleated at high supersaturation conditions, most likely before or during coalescence. As preferential growth of low–energy islands through coarsening and ripening requires high surface mobility, such a texture creation mechanism would only be active at higher temperatures. This indicates that at low temperatures, Walton's type of preferred nucleation is very unlikely to create texture.

Conversely, if the supersaturation on the surface is low (i. e. high temperature or low incidence rate) multiple adatom–adatom bonds are required for

a stable cluster. The number of adatom–adatom bonds required to create a stable cluster and how the atoms are geometrically arranged creates several possibilities, each placing a particular crystal plane parallel to the substrate. The preferred nucleation theory then posits that due to the density of clusters decreasing with cluster size, the geometrically smallest of these will become a preferred orientation in the film. These tend to place closest–packed planes parallel to the substrate.

Another view of adatom–substrate interactions has been proposed.[113] According to this view, at low growth temperatures, the conditions are so far from either surface or bulk equilibrium that kinetics limits adatoms being drawn together with nearby atoms to occupy minima in potential wells on the substrate to form two-dimensional clusters. These clusters then capture adatoms in the capture zone surrounding the nuclei and grow into columns via granular epitaxy. The size of these clusters is estimated to be approximately three interatomic diameters, based on common interatomic potentials for metals. However, it may not be meaningful to discuss orientation selection during nucleation when growth rates are above 6 nm/min, due to the extremely small critical nucleus sizes ($\sim$1 Å) the supersaturations of adatoms at such growth rates lead to.[117]

Another way texture could form early on in film growth is through growth rate anisotropies between islands with different orientations, so that by the time the film coalesces the largest grains already have a preferred orientation and continue to dominate the texture. The interface energy for a given substrate surface will generally be a strong function of the crystallographic orientation of the particle.[117] It has been proposed that the particles with minimum surface and interface energies will grow at slightly higher rates than other particles with the same volume, giving a slight growth advantage to specific orientations which minimize the surface and interface energy.[117] This pre–coalescence texture formation mechanism implicitly requires some surface mobility in the film growth system and may best describe growth at intermediate and high, rather than low, homologous temperatures.

Therefore, preferred orientations as a product of nucleation at low growth temperatures may be most applicable when nucleation barriers are high, substrates are crystalline, and growth rates are low. Both differences in texture on

different substrates or a texture placing a closest packed plane parallel to the substrate can be attributed to preferential nucleation.

3.1.3 Texture formation during coalescence of islands

Texture can form during the coarsening process in coalescence, typically resulting in the densest planes progressively becoming preferred.[116] Grain boundary motion is integral to this type of texture formation mechanism[116, 117], limiting it to temperatures high enough for grain boundary motion to be significant. During coalescence, several types of potential energy can be minimized by islands with lower energy per atom consuming others.

At sufficiently high T*, energy minimization is a proven driver of texture during film coalescence and growth. Grain boundary energy can be reduced by reducing either the total grain boundary area or favoring low–energy boundaries over high–energy boundaries.[117] Grains with low surface and interfacial energy have been found to become preferred in both experiments and in simulations.[117] A kinetic theory to account for this is that the potential energy of a crystal face scales with its potential energy, leading to a situation in which residence times are higher on low-energy surfaces, which in turn favors their growth.[116] A consequence of this is considerable surface roughness which scales with the average in-plane grain size. Such roughness could thus be used to identify films in which this texture formation mechanism has been operative.

At relatively high homologous temperatures between 0.4 and 0.5, the nuclei are liquid due to the melting point suppression in nanoscale particles, making both the coalescence and energy minimization facile.[116] Grain coarsening, or recrystallization through grain boundary migration, may also occur after island coalescence.[116]

A telltale sign of grain growth processes during film coalescence and thickening is equiaxed columnar microstructure, especially when the grain size scales with the film thickness.[117] This indicates sufficient thermal energy for the necessary grain boundary motion to have occurred. When the deposition temperature is too low for grain boundary motion to occur, microstructures tend to be non–equiaxed (such as cones growing up from the nucleation layer).[117]

Generally, grain growth dominated microstructures and textures are favored by materials with high melting point diffusivities, high growth temperatures, good film purities, and high deposition rates.[117]

3.1.4 Texture formation during film thickening

Several texture formation mechanisms that predict higher growth rates for some grains with a preferred orientation during growth of an already coalesced film have been identified, nearly all of which implicitly require sufficiently high homologous temperature for at least limited surface diffusion to be significant. Some, like recrystallization, require even higher T* in order to overcome the kinetic limitations.[117] Activation energies for surface, grain boundary, and bulk diffusion rates are typically in the ratio $1:2:4$. Thus, even at high homologous temperatures like $T^* = 0.5$, surface and grain boundary diffusion rates can still be orders of magnitude larger than bulk diffusion rates.[122] This suggests relatively few films have texture that is due to recrystallization. In homologous temperature ranges as low as $\sim 0.2 - 0.4$, surface diffusion rates can be significant, and film thickening can proceed through granular epitaxy.[116]

One texture formation model that creates preferred orientation through selective granular epitaxy is the van der Drift theory[112], which roughly states that those grains that grow fastest laterally eventually dominate the texture of the film. The film will then consist of many small grains of nearly random orientation close to the substrate, but become fiber textured close to the surface of the film, provided the film is relatively thick. In order to predict which crystals grow the fastest vertically, van der Drift uses the shape of single crystals and presents a number of cases with different types of assumptions about surface diffusion and dependence of the adatom sticking coefficient on angle of incidence.

The assumptions regarding the effect of angle of incidence may not be appropriate for CVD, where adatoms may be deposited on the surface at a different point than where the precursor molecules first impinge on the surface, especially in the case of precursors with a low sticking coefficient such as the CVD of Ru from **1**. As the angle of incidence is used in detailed computations in the predictions of all the cases except infinite surface diffusion and no

surface diffusion, only the two limiting cases seem to pertain to CVD films of ruthenium. In the case of infinite diffusion, all crystals grow in volume equally quickly, and the prediction becomes simply that the crystals with the largest height to width ratios will progressively come to dominate the film. This condition will result in three-dimensional crystals that fill the space available and form dense layers or two-dimensional needles in a columnar microstructure.

A second supersaturation-dependent texture formation theory for film thickening has been advanced by D. N. Lee.[114, 115] Lee's preferential growth model assumes only sufficient surface diffusion for adatoms on the film surface to adjust themselves to stable positions and posits that the texture of physical or chemical vapor deposits depends on whether the deposition temperature is high enough for recrystallization and on the concentration of adatoms on the surface. At the heart of the preferential growth model are the detailed kinetic implications for adatom diffusion and condensation on highly stepped and flatter surfaces. Noting that adatoms on surfaces tend to attach at steps, and that high-energy surface planes often are highly stepped, the model concludes that at high supersaturations when the adatom supply is large, the smaller average diffusion distance on highly stepped surfaces (high-energy surface planes) results in higher growth rates for high-energy surface planes. At low supersaturations, the model notes that due to a limited adatom supply, the average diffusion distance to a step no longer results in growth rate differences. On the other hand, adatom surface concentrations will differ between highly stepped surfaces and less stepped surfaces, due to the larger surface area of highly stepped surfaces. The higher adatom surface concentration on less stepped surfaces favors the growth of those low-energy surfaces.

Therefore, when there is insufficient energy for recrystallization to take place, the model suggests that the texture changes from the orientation that places the lowest surface energy crystal plane normal to the growth direction when few adatoms reside on the film surface to that orientation which places the highest energy crystal plane normal to the surface when the adatom surface concentration is high. If recrystallization is possible, the preferential growth model posits that the due to the importance of kinetics to texture formation, surface energy minimization places the minimum energy crystal plane normal to the growth direction of the film.

3.1.5 Evaluating film growth kinetics

There exists a significant body of knowledge regarding the kinetic possibilities in a homologous temperature range, contained in structure zone models. Although the structure zone models were originally developed based on different microstructure types in PVD films, their general features have been found to be rather universal and both electrodeposition and CVD exhibit analogous features to PVD films because of fundamental similarities in the deposition processes.[116, 122] Structure zone models are based on differences in mobilities at different homologous temperatures. Sticking coefficients below one and deviances from strictly normal incidence of adatoms to the surface has been shown to influence the microstructure.[122] The higher conformality of the CVD process used to deposit these ruthenium films may result in slight deviation from the PVD sputter zone models, but as the models link surface, grain boundary, and bulk mobilities with microstructures, they allow deduction of the film growth kinetics from their microstructures.

Homologous temperatures below 0.3 are referred to as zone I.[122] Zone I is characterized by low surface, grain boundary, and bulk diffusion. In zone I, microstructures are usually consist of columns separated by voids.[122] The columns are generally not single grains, but are composed of smaller, more equiaxed grains or can be completely amorphous.[116] The columns do not have to be straight, but can be nearly factal treelike dendrites.[113] The films are underdense and may have a fine fiber texture.[116] The lateral dimensions of the columns will be around 1–20 nm[113] and are set by the saturation nucleation density.[116]

At the high end of zone I temperatures and slightly above $T^* = 0.3$, the transition zone T exists. Here, crystallites are nearly random or only weakly textured.[116] Adatom surface diffusion is significant, enabling grain growth through granular epitaxy.[116] Zone T microstructures are similar to those in zone I, but without the visible boundaries between columns, and may be fractal-like.[122]

When the sticking coefficient is one, the columnar, voided microstructure is a consequence of atomic-level shadowing.[122] When the sticking coefficients are less than one, the resulting microstructure is zone T.[122] Both zone T

and zone 1 microstructure are fundamentally due to the low adatom mobility at T* < 0.3.[122] If film growth proceeds by repeated nucleation, the film will consist of nanometer-size grains arranged in a dense, non-columnar structure without faceting.[116]

In addition to the temperature, there are a number of factors that influence mobilities. Strength of interatomic bonds is one. Even at room temperature, the mobility of adatoms on the growing film and on the substrate may not be the same.[113] If the film-substrate bonding is weaker than the interatomic bonding of the film, texture creation mechanisms that rely on adatom mobility on the substrate may still be operational.[113] Another is the presence of impurities. Even low levels of impurities may act as grain refiners, which encourage renucleation, resulting in small nanometer-range grain sizes due to blocking of coarsening.[116] Impurities may also decrease both surface and grain boundary mobilities, encouraging zone I-type structures.[116]

At higher temperatures, zone II extends from 0.3 to 0.5. and zone III extends from 0.5 and up. In zone II, surface diffusion is active, although microstructures are still columnar.[122] In zone III, bulk diffusion is possible, leading to equiaxed grains.[122]

The melting point of ruthenium is 2607 K, or 2334 °C. This means that for Ru, zone I extends from room temperature to 500 °C, zone II runs up to 1030 °C, and zone III reaches beyond that. All low-temperature growth of ruthenium films falls in zone I.

3.2 Experimental

3.2.1 Texture characterization

In order to gain insight into the possible mechanisms of texture formation and evolution in CVD films grown at low temperatures from **1**, films were grown to similar thicknesses at different temperatures on an epitaxially matched[84] crystalline substrate (sapphire), a non-epitaxial crystal (Si (0 0 1)), and an amorphous substrate (thermally grown SiO_2).

Standard 2θ–ω X–ray diffraction (XRD) and glancing angle X–ray diffraction (GAXRD) patterns were collected on a Philips X'Pert 2 system using Cu

Kα radiation in order to determine the out-of-plane texture. GAXRD at a constant glancing angle of 1° relative to the crystal planes most nearly parallel to the surface was performed in addition to standard 2 θ–ω scans. Glancing angle measurements eliminate peaks due to the substrate because the X-ray beam enters the substrate only to a small extent, and also gives a greater signal to noise ratio because the beam interacts with a larger volume of film. Nanodiffraction patterns of films directly deposited onto SiO_x membranes were taken with a JEOL 2010 F transmission electron microscope in nanobeam mode. The morphology and microstructure were studied by examining cross-sections of films in a Hitachi S–4700 scanning electron microscope.

Quantification of any in-plane texture was not possible in a reasonable amount of time for any of the films tried. Pole figure intensities were too low to give clear information. However, the out-of-plane texture was quantified by calculating texture coefficients for each resolved reflection. Texture coefficients are defined as[123, 124]

$$C_i = \frac{N\frac{I_i}{I_0}}{\sum_{i=1}^{N}\frac{I_i}{I_0}}, \tag{3.1}$$

where C_i is the texture coefficient for reflection *i*, N is the number of reections considered, I_i is the intensity in film of reection *i*, and I_{i0} is the intensity of reection *i* in a randomly oriented sample. In most cases, lms had more than one preferred orientation. $(0\,0\,0\,1)$ was the most preferred orientation in almost all films grown at temperatures below 350 °C, while its prominence diminished above 350 °C. The overall degree of texture in the films, σ, was computed from a close analogue to the standard deviation as

$$\sigma = \sqrt{\sum_{i=1}^{N}\frac{(C_i - C_{i0})^2}{N}}, \tag{3.2}$$

where C_i and N are defined as in equation 3.1 and C_{i0} is the texture coeffcient of a peak in a randomly oriented film. As can quickly be seen from the denition, σ is zero for a randomly oriented film. σ values of 1 or above are considered highly textured.

3.3 Results

3.3.1 *Films grown on amorphous silicon dioxide*

Under a homologous temperature of 0.25 (380 °C), the films exhibit a sharp preference for grains with the $(0\,0\,0\,1)$ basal plane oriented parallel to the substrate. At T* = 0.26 (400 °C), this preference disappears and is replaced by a weak preference for $(1\,1\,\bar{2}\,2)$ and $(1\,0\,\bar{1}\,1)$. As the homologous temperature is raised to 0.28 (450 °C), $(0\,0\,0\,1)$ joins $(1\,1\,\bar{2}\,2)$ and $(1\,0\,\bar{1}\,1)$ as a somewhat preferred orientation again, although the degree of preference is not nearly as high as at lower temperatures. (Figure 3.2.)

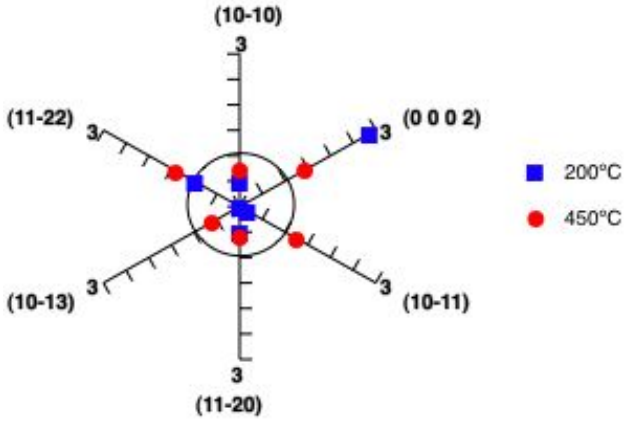

Figure 3.2: Texture coefficients for hexagonal ruthenium films grown on amorphous silicon dioxide at a homologous temperatures of 0.18 (200 °C) and 0.28 (450 °C). Values over 1, indicated by the circle, indicate a preferred direction. The film grown at 200 °C is 65 nm thick, and the 450 °C film is 81 nm thick.

The films are crystalline with small grain sizes and thicken through repeated renucleation. The microstructure is composed of relatively featureless dense layers at all growth temperatures with no visible voids, typical of a zone T microstructure showing no faceting. This may be due to the low sticking coefficient of the precursor compared to PVD adatoms and to the nanocrystalline nature of the films, clearly visible in TEM micrographs. (Figure 3.3.) Grain refinement through impurities is very likely, since the films contain a

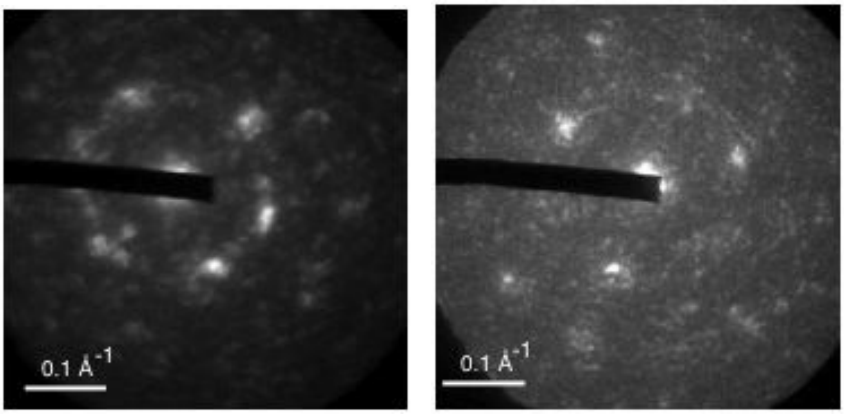

(a) TEM nanodiffraction pattern from nanometer–sized area in 183 nm thick Ru film grown from **1** at T* = 0.20 (250 °C).

(b) TEM nanodiffraction pattern from nanometer–sized area in 146 nm thick Ru film grown from **1** at T* = 0.28 (450 °C).

Figure 3.3: TEM nanodiffraction patterns of thick Ru films grown at a high and a low temperature.

significant amount (∼30 at. %) of carbon. The average grain size at 170 °C is 20 ± 6 nm, and at 400 °C it is 40 ± 3 nm. The small grain sizes together with the microstructure suggest film growth through renucleation and grain refinement by impurities, as well as a near complete lack of grain growth during coalescence.

3.3.2 Films grown on crystalline silicon

Below homologous temperatures of 0.2 (250 °C), the films exhibit a sharp preference for grains with the $(0\,0\,0\,1)$ basal plane oriented parallel to the substrate, as on amorphous substrates. Above T* = 0.2 (250 °C), the preference for $(0\,0\,0\,1)$ orientation disappears. (Figure 3.4.) At T* = 0.22 (300 °C), the $(1\,1\,\bar{2}\,2)$ and $(1\,0\,\bar{1}\,1)$ orientations become somewhat preferred. At T* = 0.26 (400 °C), $(1\,0\,\bar{1}\,1)$ is moderately preferred while $(1\,1\,\bar{2}\,2)$ is somewhat preferred. At T* = 0.28 (450 °C), $(1\,1\,\bar{2}\,2)$ and $(1\,0\,\bar{1}\,1)$ are both only somewhat preferred. Grain sizes are similar to those on amorphous substrates at a T* of 0.19 (220 °C; 10 ± 6 nm) and increase somewhat to 70 ± 8 nm at a T* of 0.28 (450 °C). As on amorphous substrates, this suggests continual renucleation during thickening.

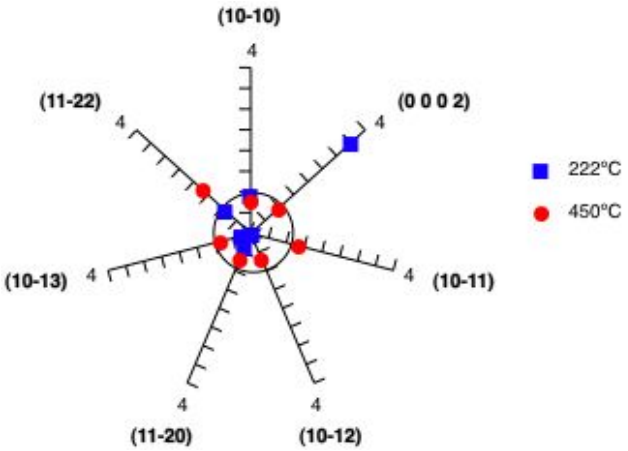

Figure 3.4: Texture coefficients for hexagonal ruthenium films grown on face-centered cubic silicon at homologous temperatures of 0.19 (220 °C) and 0.28 (450 °C). Values over 1, indicated by the ring, indicate a preferred direction. At 220 °C, the film thickness is 120 nm. At 450 °C, the thickness is 216 nm.

The microstructures of the films grown on silicon are compact and globular due to their small grain size, lending few additional clues to the crystal growth kinetics during growth. As the texture on amorphous and FCC substrates were very similar, the differences in microstructure between films grown on silicon and on silicon dioxide are more likely due to the differences in nucleation chemistry, discussed in chapter 2.

3.3.3 Films grown on c–plane sapphire

C–plane sapphire is an epitaxial substrate for ruthenium.[84] At a homologous temperature of 0.18 (200 °C), the films grown on sapphire are $(0\,0\,0\,1)$ textured. As the homologous temperature is slightly increased to 0.22 (300 °C), the sharp preference for the $(0\,0\,0\,1)$ orientation declines to a slight preference as $(1\,0\,\bar{1}\,0)$ and $(1\,1\,\bar{2}\,2)$ also are somewhat preferred orientations, but reappears strongly at a T* of 0.30 (500 °C), although $(1\,0\,\bar{1}\,1)$ and $(1\,0\,\bar{1}\,3)$ are also somewhat preferred. (Figure 3.5.) The occurrence of $(1\,0\,\bar{1}\,0)$ as a preferred orientation in addition to the epitaxial orientation and the other orientations that were pre-

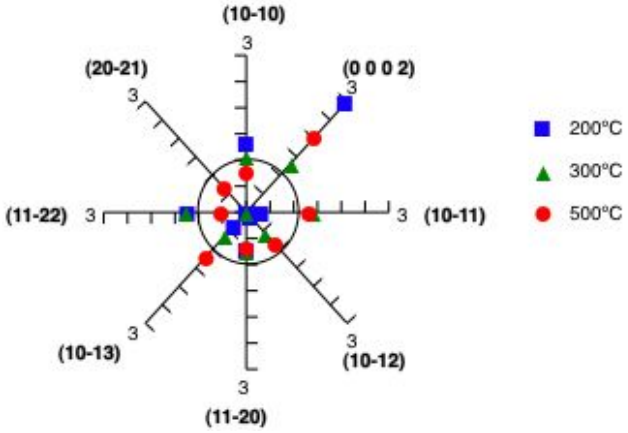

Figure 3.5: Texture coefficients for hexagonal ruthenium films grown on hexagonal c–plane sapphire at homologous temperatures of 0.18 (200 °C), 0.22 (300 °C), and 0.30 (500 °C). Values over 1, indicated by the ring, indicate a preferred direction. The film thicknesses are 202 nm (200 °C), 157 nm (300 °C), and 96 nm (500 °C).

ferred on SiO_2 and silicon substrates is noteworthy, as the $\{1\,0\,\bar{1}\,0\}$ planes are the prismatic planes of the hexagonal cell. Also noteworthy is that the sapphire was the only substrate on which films displayed a strong $(0\,0\,0\,1)$ preference at high temperatures as well as low temperatures.

Grain sizes are similar to those on SiO_2 and Si substrates at a T* of 0.18 (200 °C; 20 ± 6 nm), but jump an order of magnitude to $\sim 200 \pm 2$ nm at a T* of 0.26 (400 °C) and above. Above this temperature, the crystallographic grains are roughly twice the film thickness. The microstructures of the ruthenium films on sapphire substrates change markedly from featureless and compact to rocky–looking at a homologous temperature of 0.26 (400 °C). (Figure 2.14.) The change in microstructure coincides with the increase in grain size and a marked drop in growth rate from 14 – 25 nm/min below T* = 0.26 to 1 nm/min above, and may reflect a shift away from thickening by continual renucleation to granular epitaxy.

3.3.4 *Overall degree of texture*

The overall degree of texture (equation 3.2) supports considering the texture coefficients by providing an overview of all texture coordinates in a film. Regardless of substrate, for films grown below T* = 0.24 (350 °C) σ hovers around one, followed by a sharp decline above that temperature. (Figure 3.6.)

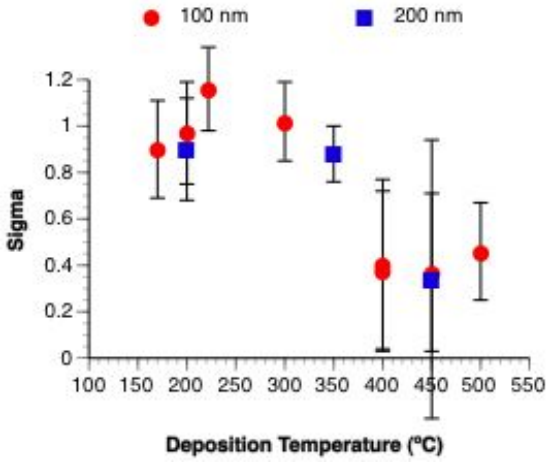

Figure 3.6: The overall degree of texture, σ, as a function of deposition temperature, for 100 nm and 200 nm thick films deposited on silicon(1 1 0), Al_2O_3 (0 0 0 1), and thermally grown SiO_2.

The large uncertainties, especially above homologous temperatures of 0.24 (350 °C), reflect the presence of several slightly preferred orientations and only slight underpreference of others and carry information about the degree of texture in and of itself (or lack thereof) rather than strictly the quality of the underlying data. The uncertainty in individual texture coefficients is typically in the 1–3% range for sharply preferred orientations and in the 10–20% range for relatively dispreferred orientations.

3.3.5 *Growth temperature modulation*

When the growth temperature is modulated, the final growth temperature mostly determines the texture, although some effect of early growth stages may

be seen. (Figure 3.7.) This is consistent with film thickening through renucleation rather than granular epitaxy.

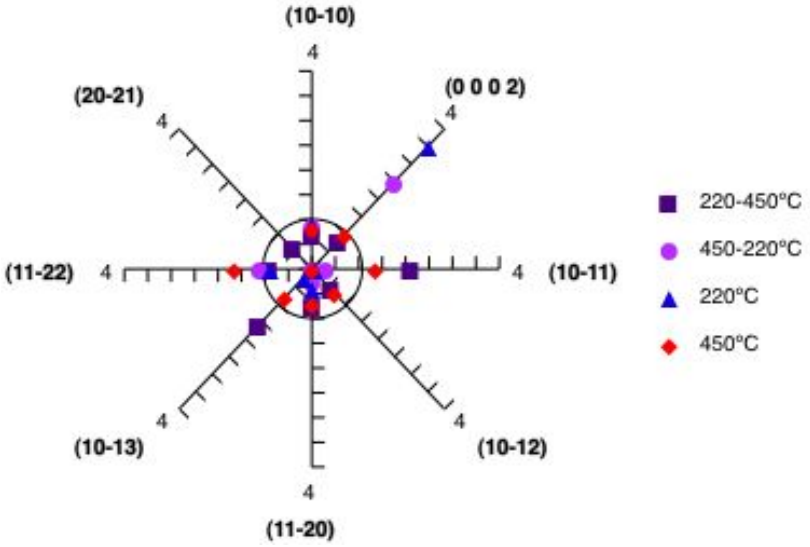

Figure 3.7: Texture coefficients for ruthenium films nucleated at one temperature and thickened at another. The texture coefficients of single-temperature films at 220 °C and 450 °C are shown for reference. The low–high temperature modulated film was 172 nm thick. The high–low temperature modulated film was 183 nm thick.

The overall texture coefficient in the film that was nucleated at 220 °C and thickened at 450 °C was only 0.52 ± 0.42, significantly lower than the 1.16 ± 0.18 seen in films grown only at 220 °C. The effect of the growth temperature increase was not only to lower the overall degree of texture, but also to change which orientations were preferred as well as the microstructure. Instead of exhibiting sharp $(0\,0\,0\,1)$ texture, the low-high temperature modulated film exhibited two preferred orientations: $(1\,0\,\bar{1}\,1)$ and $(1\,0\,\bar{1}\,3)$. $(1\,0\,\bar{1}\,1)$ was strongly preferred, whereas $(1\,0\,\bar{1}\,3)$ was only moderately preferred. Further, it is interesting to note that the most preferred orientation in single–temperature films grown at 450 °C was $(1\,1\,\bar{2}\,2)$, which is slightly dispreferred in the temperature–modulated film. $(1\,0\,\bar{1}\,1)$ was slightly preferred in single temperature films grown at 450 °C, but was sharp in the temperature–modulated film.

The microstructure, like the texture, of this temperature-modulated film is unique. Instead of being compact, the microstructure consists of feathery, almost fractal–like columns rising from a compact layer, typical of zone I rather than zone T. (Figure 3.8.) The visibly columnar microstructure clearly indicates that a homologous temperature of 0.28 is too low for grain boundary mobilities to be significant. The grain size was roughly the same as in films grown only at 450 °C, an order of magnitude larger than the nanometer-size grains in films grown at 220 °C. Together with the sharp preference for an unusual orientation, the microstructure and grain size also suggest that granular epitaxy may have contributed to the thickening of the film at the higher temperature.

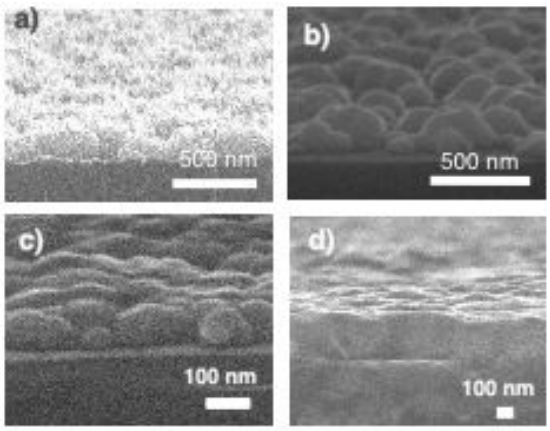

Figure 3.8: Microstructures of temperature–modulated ruthenium films (nucleated at one temperature and grown at another) on silicon substrates, compared to films grown and nucleated at one temperature. a) 172 nm thick film nucleated at 220 °C, thickened at 450 °C; b) 183 nm thick film nucleated at 450 °C, thickened at 220 °C; c) 120 nm thick film nucleated and grown at 220 °C; d) 216 nm thick film nucleated and grown at 450 °C.

The overall texture coefficient in the temperature modulated film that was nucleated at 450 °C and thickened at 220 °C was 0.80 ± 0.27, which is significantly higher than the value of 0.34 ± 0.60 seen in single–temperature films grown at 450 °C. The effect of the growth temperature drop was not only to more than double the overall degree of texture and make the $(0\,0\,0\,1)$ plane more than twice as preferred as the second most preferred orientation, but to

create a globular microstructure very similar to that seen at 220 °C. (Figure 3.8) In the temperature modulated film nucleated at 450 °C and thickened at 220 °C, $(0\,0\,0\,1)$ orientation was sharply preferred, but $(1\,1\,\bar{2}\,2)$ was also slightly preferred. These two orientations are the generally speaking the most preferred orientations at low and high temperatures, respectively.

3.3.6 Evolution of texture with thickness

Due to the low signal intensities of films thinner than ∼50 nm and the grain size broadening in films with small grain sizes, gathering XRD diffractograms of very thin films was only feasible at high growth temperatures where the grain sizes are large enough to give clear peaks even at small thicknesses. At 500 °C on c–plane sapphire substrates, even a ∼30 nm film gives sufficient signal intensity to calculate texture coefficients. Comparing the texture coefficients of a thin and thick film grown at the same temperature, clear evidence of texture development during film growth emerges. When the films are around 30 nm thick, there are four preferred directions. By the time the films reach ∼100 nm, only two of them remain preferred, but a third previously unpreferred orientation now dominates the film. (Figure 3.9.)

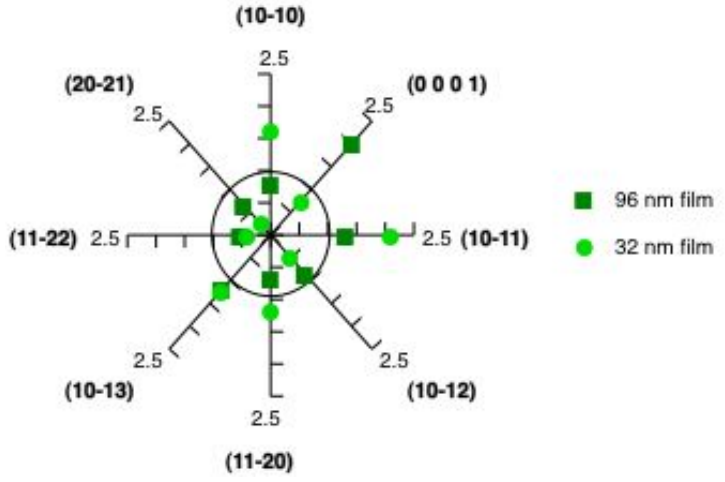

Figure 3.9: Texture coefficients of a thick and a thin film grown at 500 °C on sapphire substrates. The ring indicates 1 on all axes.

In the 32 nm thick film the preferred orientations are $(1\,0\,\bar{1}\,0)$, $(1\,0\,\bar{1}\,1)$, $(1\,1\,\bar{2}\,0)$, and $(1\,0\,\bar{1}\,3)$. The first two of these are sharply and moderately preferred, respectively. In the 96 nm thick film, $(0\,0\,0\,1)$ is sharply preferred, while $(1\,0\,\bar{1}\,1)$ and $(1\,0\,\bar{1}\,3)$ remain somewhat preferred. This suggests that even with several initial other preferred orientations, film thickening creates $(0\,0\,0\,1)$ oriented grains preferentially. This clearly demonstrates texture development with growth, rather than during nucleation or coalescence. The $(0\,0\,0\,1)$ orientation is more strongly preferred at high temperatures on sapphire substrates than on either FCC silicon or amorphous silicon dioxide, possibly due to it being the epitaxial orientation. This indicates that even when impurities interfere with the epitaxial interface registry between film and substrate, epitaxially aligned grains may become favored during thickening.

3.4 Discussion

The development of texture as a function of thickness and the influence of the final growth temperature in the temperature modulated films suggest that the final texture is formed during thickening of the films, rather than during nucleation or coalescence. This is expected at such low homologous temperatures, where grain boundary and bulk mobilities will be negligible. In accordance with this expectation, there is very little indication from the microstructures of the films that surface diffusion was significant, and no indication that grain boundary or bulk diffusion was possible.

That the trend of high texture at low temperatures followed by a reduction in texture at higher temperatures, holds on all substrates suggests that the role of the substrate in creating the low-temperature texture is minimal, despite evidence in individual texture coefficients for influence of an epitaxial substrate. The similar texture behavior at both 100 and 200 nm thicknesses also suggest that any thickness dependence of texture is operative at thicknesses under 100 nm, which is consistent with the thickness study on sapphire.

At low temperatures, there was very little difference in textures on any substrates. Films on all three substrates exhibited a $(0\,0\,0\,1)$ texture at low temperatures which was lost slightly above a T* of 0.2. While there may be initial

local pseudomorphic epitaxy on silicon, the influence will not last long and is unlikely to be strong or significant. The small grain sizes, the high impurity contents, and the presence of the same texture on other substrates at these temperatures on sapphire suggest that interfacial registry is not responsible for the low–temperature texture on sapphire substrates.

Above homologous temperatures of 0.2, $(1\,1\,\bar{2}\,2)$ and $(1\,0\,\bar{1}\,1)$ were preferred orientations both on amorphous SiO_2 and FCC silicon substrates, suggesting a common formation mechanism. While $(1\,1\,\bar{2}\,2)$ was also a preferred direction in films on sapphire substrates, $(0\,0\,0\,1)$ remained preferred, and $(1\,0\,\bar{1}\,0)$ was also preferred. This suggests competing effects on sapphire substrates: one resulting in $(1\,1\,\bar{2}\,2)$ being preferred, another due to interface registry that favors $(0\,0\,0\,1)$ and $(1\,0\,\bar{1}\,0)$.

As the homologous temperature approaches 0.3, $(0\,0\,0\,1)$ reappears as a preferred orientation on SiO_2 substrates and becomes strongly preferred on sapphire substrates, but not silicon substrates. $(1\,1\,\bar{2}\,2)$ is also preferred on silicon dioxide and silicon substrates, while $(1\,0\,\bar{1}\,1)$ is the only preferred direction present in all films grown close to $T^* = 0.3$. This suggests that all three planes became preferred by a common mechanism. The higher temperatures together with the significantly larger grain sizes on sapphire compared to Si and SiO_2 indicate that interfacial registry effects may influence the texture toward $(0\,0\,0\,1)$, although no further than fiber texture.

Understanding why the texture develops during thickening and determining the mechanism requires considering the kinetic limitations at each film growth stage. Textures placing close-packed planes parallel to the substrate, as observed at low temperatures, can form during nucleation and coalescence. However, the kinetic limitations at low growth temperatures rule out those texture formation mechanisms.

Texture formation during nucleation is favored by high nucleation barriers, crystalline substrates, and low growth rates. The nucleation barriers on all substrates are low, and the preferred nucleation theory inherently suggests that at low temperatures preferred nucleation is unlikely to create texture. If surface mobilities were high enough, energy minimization of islands could create texture before coalescence. However, the orientation the films have is the maximum energy orientation, showing that energy minimization is kinetically

hindered in creating texture during nucleation.

Texture creation during coalescence requires grain boundary motion, which was not possible at even the highest growth temperatures used. There was little evidence for coarsening during coalescence or film growth, and the relatively high carbon content in the films also suggests that coarsening during coalescence is not responsible for the texture in this case.

Kinetic considerations also aid in understanding the texture formation during thickening. Van der Drift's theory requires significant surface diffusion, which may be possible at homologous temperatures close to 0.3. At the lower end of the deposition temperature range, surface diffusion is unlikely to be high enough to enable van der Drift's theory to apply. In contrast, Lee's preferential growth theory requires only modest surface diffusion, and predicts that in the high supersaturation (low T*) case, the highest energy surface plane will be parallel to the surface. At low temperatures, this is what is observed on all substrates.

Orientation	**Height/Width Ratio**
$(1\,0\,\bar{1}\,0)$	1.15
$(0\,0\,0\,1)$	1.58
$(1\,0\,\bar{1}\,1)$	1.58
$(1\,0\,\bar{1}\,2)$	0.79
$(1\,1\,\bar{2}\,0)$	1.15
$(1\,0\,\bar{1}\,3)$	0.53
$(1\,1\,\bar{2}\,2)$	3.16

Table 3.1: Grain height to width ratios for ruthenium, identified by crystal plane perpendicular to growth direction (along the z axis in figure 3.1.) The prediction in the case of infinite surface diffusion of the van der Drift theory is that grains with higher height to width ratios will grow at the expense of those with lower ratios.

At higher temperatures, both the van der Drift theory and the preferential growth model could apply. The prediction of the van der Drift theory at higher temperatures is that the $(1\,1\,\bar{2}\,2)$ orientation should be most preferred, followed by $(1\,0\,\bar{1}\,1)$ and $(0\,0\,0\,1)$. (Table 3.1.) These are the three directions observed at high growth temperatures. However, the results do not follow van der Drift's predictions in detail: $(1\,1\,\bar{2}\,2)$ is the most preferred orientation at high temper-

atures on silicon substrates, but is not preferred on sapphire substrates, and is preferred approximately equally with $(0\,0\,0\,1)$ and $(1\,0\,\bar{1}\,1)$ on silicon dioxide. The discrepancy in details may be due to the difference between the assumptions of the van der Drift model (infinite diffusion, no substrate influence on texture) and the somewhat more complicated situation in reality. Nevertheless, the van der Drift model qualitatively describes the texture at high deposition temperatures.

The preferential growth theory predicts that the favored orientation should place the minimum energy planes parallel to the surface at low supersaturations (high T*). Among the orientations observed, $(1\,1\,\bar{2}\,0)$ is the minimum surface energy plane.[120] While $(1\,1\,\bar{2}\,2)$, $(1\,0\,\bar{1}\,1)$ and $(0\,0\,0\,1)$ were often preferred orientations at higher temperatures, $(1\,1\,\bar{2}\,0)$ was never observed to be preferred. On the contrary, at the high end of the growth temperature range $(1\,1\,\bar{2}\,0)$ was found to be the most disfavored orientation on silicon dioxide substrates as well as silicon substrates and among the most disfavored on sapphire substrates.

The low–high temperature modulated film is not well described by the van der Drift theory, despite other characteristics of the film being largely similar to the films grown at higher temperatures. The lack of $(1\,1\,\bar{2}\,2)$ preference together with the preference for $(1\,0\,\bar{1}\,3)$ orientation is not consistent with the predictions of the van der Drift theory. The preferential growth model also fails to predict the sharp preference for $(1\,0\,\bar{1}\,1)$, as $(1\,1\,\bar{2}\,0)$ is the minimum energy plane for ruthenium. Low temperature films and nanostructures cannot relax toward equilibrium, and often reflect their synthesis route. In this case, it is likely that the interplay between the initial low temperature nucleation layer and the higher growth temperature creates a more complicated texture formation situation than either theory can predict in detail, also indicated by the unique microstructure. Despite this, the texture formation in the films is consistent with the preferential growth theory at homologous temperatures below approximately 0.2 and the van der Drift model at homologous temperatures above that.

CHAPTER 4

Low–Temperature CVD of Manganese Nitride Thin Films

4.1 Introduction

Manganese nitrides are fascinating materials that deserve intense study.[125, 126] The tetragonal η–Mn_3N_2 phase adopts a slightly distorted cubic (rock salt) structure in which one-third of the octahedral nitrogen sites are vacant.[126] In contrast, the hexagonal ξ phase is compositionally-broad and encompasses stoichiometries such as Mn_5N_2, Mn_2N, and $Mn_2N_{0.86}$.[126] The physical properties of manganese nitrides are even more interesting: Mn_4N is ferrimagnetic[127], Mn_3N_2 and MnN are antiferromagnetic[128, 129], and η-Mn_3N_2 is a metallic conductor and may be a superconductor above 4 K.[130] In addition, manganese-doped gallium nitride, $Ga_{1-x}Mn_xN$, which is a magnetic semiconductor at room temperature[131, 132], is an attractive material for the storage and transport of spin in spintronic devices; $Ga_{1-x}Mn_xN$ also has potential applications in electronics and optoelectronics.[133]

Part of the reason manganese nitrides have received less attention than they deserve is that they are relatively difficult to synthesize. Although films of η–Mn_3N_2 have previously been deposited by molecular beam epitaxy[134], to the best of our knowledge, no chemical vapor deposition processes for pure manganese nitrides have been reported. CVD has been used, however, to deposit thin films of manganese–doped gallium nitride by adding a Mn–containing precursor such as manganocene, $Mn(C_5H_5)_2$ to a CVD process for depositing GaN.[131, 135–137] The required growth temperatures are high, between 800 and 1100 °C.

CVD growth of transition metal nitride phases is often best accomplished

from a mixture of ammonia and a transition metal dialkyamide precursor. For example, TiN films can be grown in this way from the precursor tetrakis(dimethylamido)–titanium.[138–142] In the absence of ammonia, the deposited films are severely carbon-contaminated owing to reactions that generate M–N–C rings.[139, 140, 142]. When NH_3 is provided as a co–reactant, however, a transamination reaction occurs in which the dialkyl amide ligands react with ammonia to form dialkylamine and species with M–NH_x functional groups.[140] The latter cleanly transform into largely carbon–free metal nitride films.

For manganese nitride, few manganese amides are known, and of these only one is volatile: bis(trimethylsilyl)amidomanganese(II).[143] Due to the relatively large size of the Mn^{II} ion, large sterical bulk is required to prevent precursor dimerization or even polymerization. This complex, which is dinuclear in the solid state despite the large steric bulk of the amide ligand[144, 145], has been used to grow films of elemental manganese.[143]

The investigation of the chemistry of the even more sterically bulky ligand bis(di–*tert*)butyl)amide has recently begun.[146] Here, the CVD from two–coordinate bis[di(*tert*)–butyl)amido]manganese(II) (**2**, figure 4.1) is reported and the effect that ammonia has on the thin film growth examined.

4.2 Experimental

4.2.1 Chemical vapor deposition studies

The films were deposited in a previously described chamber[36] of ultra–high vacuum construction with a base pressure of $5 \cdot 10^{-9}$ Torr at total pressures ranging from 1.5 – 2.6 mTorr. Quadrupole mass spectrometry of the gases in the chamber before film growth indicates that the majority of the background is dihydrogen, which is inefficiently pumped by the turbopump. Deposition temperatures were measured using a k–type thermocouple for all temperatures except 300 °C and above, for which an infrared pyrometer (Omega) was used. Substrates were heated up to 200 °C by radiative heating from a tungsten filament. At and above 300 °C, silicon substrates were heated directly by Joule heating. Insulating substrates were clamped over a Joule-heated silicon backing plate. The temperature inhomogeneity when using resistive heating is

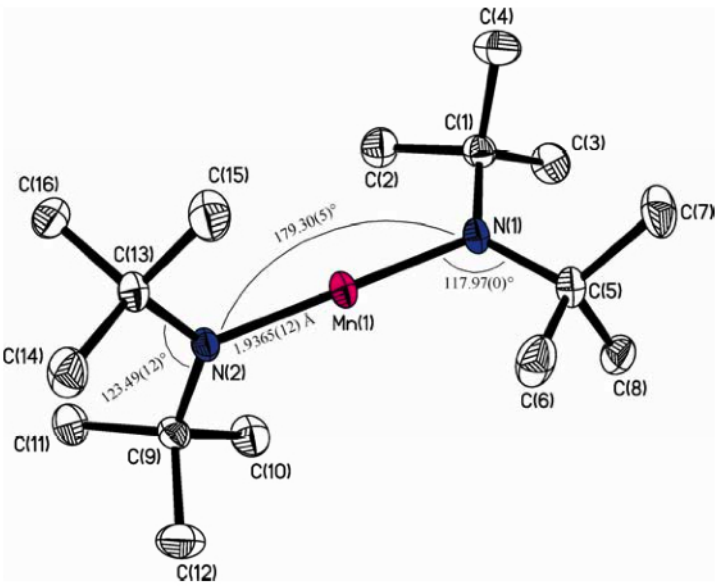

Figure 4.1: Structure of the chemical vapor deposition precursor bis[di(*tert*)–butyl)amido]manganese(II), **2**.

estimated to be $\pm$ 10 °C. The precursor was kept at 40 °C, and was delivered from the stainless steel reservoir to the substrate using 10 sccm dinitrogen as a carrier gas. The delivery lines were not heated. Control experiments showed that the nitrogen carrier gas was unreactive toward the precursor. Growth was monitored in–situ with a spectroscopic ellipsometer (J. A. Woollam Co.).

Manganese nitride films were grown on degenerately doped *n*–type Si(1 0 0) (SiliconQuest International), plasma-deposited amorphous carbon on Si(1 0 0), and holey carbon transmission electron microscope (TEM) grids (SPI). Immediately before use, all substrates except the TEM grids were cleaned ultrasonically by successive immersion in trichloroethane, acetone, isopropanol, and deionized (DI) water. The silicon substrates were rinsed in 10% hydroflouric acid solution to remove the native oxide. Films were grown between 80 °C and 300 °C at precursor partial pressures of 0.02 – 0.06 mTorr. However, the precursor was delivered through a tube of 3.8 mm inside diameter pointed directly at the substrate. Due to gas expansion effects into vacuum, the local flux

is considerably larger than the average pressure of the chamber. Ammonia fluxes ranged from 1 to 40 sccm, resulting in chamber ammonia partial pressures of 0.02 – 0.36 mTorr. Select films were annealed in vacuum with no prior air exposure at 500 °C (as measured by pyrometer) for two hours.

Manganese films were also grown on degenerately doped *n*–type Si(1 0 0) (SiliconQuest International) and *n*–type Si(1 0 0) covered with 200 nm of evaporated chromium, deposited to minimize nucleation delays. Films were grown between 300 °C and 600 °C at partial pressures of 0.025 – 0.004 mTorr.

4.2.2 Film characterization

Standard $2\,\theta$–ω X–ray diffraction (XRD) and glancing angle X–ray diffraction (GAXRD) patterns were collected on a Philips X'Pert 2 system using Cu Kα radiation. GAXRD at a constant glancing angle of 1°relative to the crystal planes most nearly parallel to the surface was performed in addition to standard $2\,\theta$–ω scans. Glancing angle measurements eliminate peaks due to the substrate because the X–ray beam enters the substrate only to a small extent, and also gives a greater signal to noise ratio because the beam interacts with a larger volume of film.

Fracture cross-sectional high resolution scanning electron microscopy (SEM) micrographs were obtained on a Hitachi S–4700 scanning electron microscope. Auger electron spectra (AES) were collected on a Physical Electronics PHI 660 scanning Auger microprobe, and X–ray photoelectron spectra (XPS) were obtained on a Kratos Axis ULTRA spectrometer. Due to rapid oxidation, the compositions of the manganese films were determined immediately ($\sim$3 minutes of air exposure). Surface topographies were determined with a Digital Instruments Dimension 3100, using a Nanoscope 3A controller in tapping mode. BudgetSensors TAP300A1 tips were used. Brightfield images and diffraction patterns of the films grown on TEM grids were taken using a JEOL 2100 transmission electron microscope and a JEOL 2010F scanning transmission electron microscope in STEM, TEM, and nanobeam mode using probe sizes of 2.6 and 7.0 nm.

4.3 Results and discussion

4.3.1 Film phases

Specular, bronze-colored films can be deposited from $Mn[N(t\text{–}Bu)_2]_2$, **2**, in the presence of ammonia at temperatures as low as 80 °C. Remarkably, even at these low growth temperatures, the films are crystalline. (Figure 4.2.) Between 80 °C and 200° , the XRD diffractograms show that the crystalline phase present is tetragonal η–Mn_3N_2. The cell parameters obtained, $a = 2.985 \pm 0.056$ and $c = 12.016 \pm 0.042$ Å are consistent with all reported literature values for η–Mn_3N_2. ($a = 2.971 \pm 1$, $c = 12.128 \pm 5$ Å[126]; $a = 2.974$, $c = 12.126$ Å[128]) At 300 °C , several phases were observed and indexed in the diffractogram: tetragonal η–Mn_3N_2, hexagonal ξ-phase $Mn_2N_{1.08}$ and cubic $Mn_{23}C_6$. Taking elemental composition into account (see below), the film consists very roughly of 40 atomic percent $Mn_2N_{1.08}$, 40 atomic percent Mn_3N_2, and 20 atomic percent $Mn_{23}C_6$. The film grain size, calculated from the Scherrer equation, increases from 10 nm at 80 °C to 23 nm at 200 °C, but then decreases to 10 nm at 300 °C for the multiphase material (figure 4.3). At 200 °C, the η–Mn_3N_2 grain size increases from 10 to 20 nm as the ammonia flux increases from 1 to 4.3 sccm; at higher fluxes the grain size decreases slightly. (Figure 4.4.)

In all of the films, the crystal grains are preferentially oriented with the (1 0 0) plane nearly parallel to the film surface. On average, the films had an overall texture coefficient (defined in equation 3.2) around 0.8, making the films significantly textured. (Figure 4.5.) Although the uncertainty in σ is relatively large, most of the films had σ values between moderate and high degree of texture.

Annealing a film grown at 200 °C and an ammonia flux of 5 sccm for 120 minutes at 500 °C did not increase σ, but eliminated the XRD peak due to the (1 0 0) plane and increased the texture coefficient (defined in equation 3.1) of the (1 1 0) plane. Annealing increased roughness nearly tenfold from 2.30 nm (figure 4.6(c)) to 21.04 nm (figure 4.6(d)) and nearly doubled grain size from 21.8 ± 1.9 nm to 40.4 ± 4.2 nm.

The correlation between the increase in roughness, grain size increase, and texture increase suggests that (1 1 0) grains grow faster than other grains. This

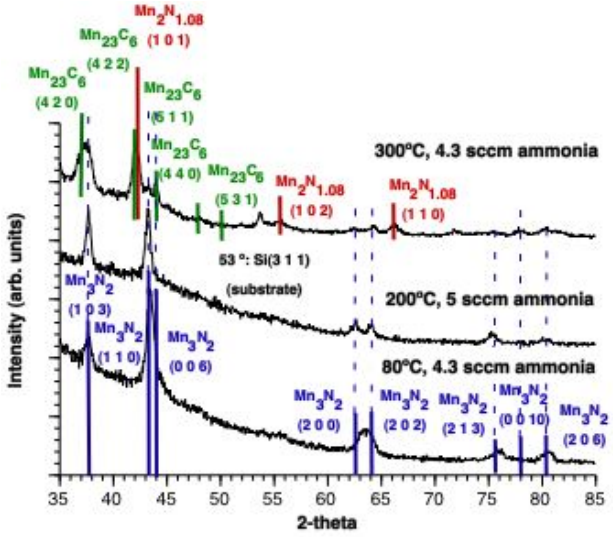

Figure 4.2: X–ray diffractograms of manganese nitride films grown from **2** at 80 °C (bottom), 200 °C (middle), and 300 °C (top) at ammonia fluxes of 4.3 and 5 sccm. The η–Mn_3N_2, $Mn_2N_{1.08}$, and $Mn_{23}C_6$ reflections are indicated.

is consistent with the van der Drift theory of texture formation[112], which states that, for the case of infinite surface diffusion, those grains that grow fastest laterally eventually dominate the texture of the film. For a tetragonal material with $c\,/\,a > \sqrt{2}$, such as η–Mn_3N_2, the van der Drift theory predicts that the <1 0 0> direction grows the fastest, which places the (1 1 0) plane parallel to the surface, as we see experimentally for the Mn_3N_2 films.

The films grown at 100 °C and an ammonia flux of 5 sccm consist of crystal grains of η–Mn_3N_2 embedded in an amorphous matrix. Brightfield TEM micrographs show amorphous regions (figure 4.7, area 1) in addition to crystal grains (figure 4.7, area 2). Nanodiffraction patterns give similar results. Simple estimation of crystallite volume fraction (estimating crystallite density, then estimating crystallite area) yields 23% crystallites.

In contrast, the films grown at 200 °C in an ammonia flux of 5 sccm are nearly completely crystalline. Brightfield TEM micrographs show that crystalline grains abut one another in a dense structure, with no intervening amorphous material. (Figure 4.8.) The TEM–derived diffraction patterns show that

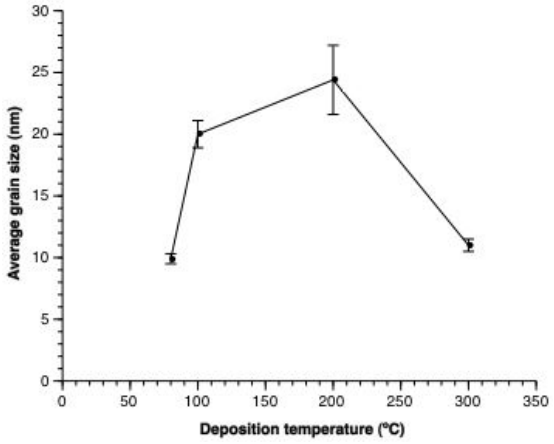

Figure 4.3: Grain size versus growth temperature for manganese nitride films grown from 1 and 4.3 sccmof ammonia.

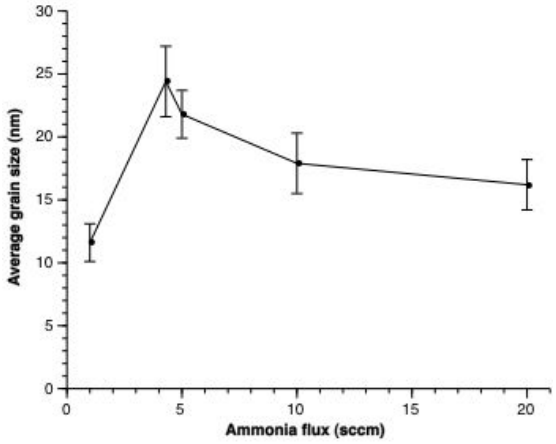

Figure 4.4: Grain size vs. ammonia flux for manganese nitride films grown from **2** at 200 °C.

the films are polycrystalline, in agreement with the XRD results. Plane indexing from high-quality diffraction patterns is consistent with the same tetragonal cell calculated by XRD, and confirms that the films are composed of crystalline η–Mn_3N_2. (Figure 4.8 inset) Nanodiffraction patterns, taken from many

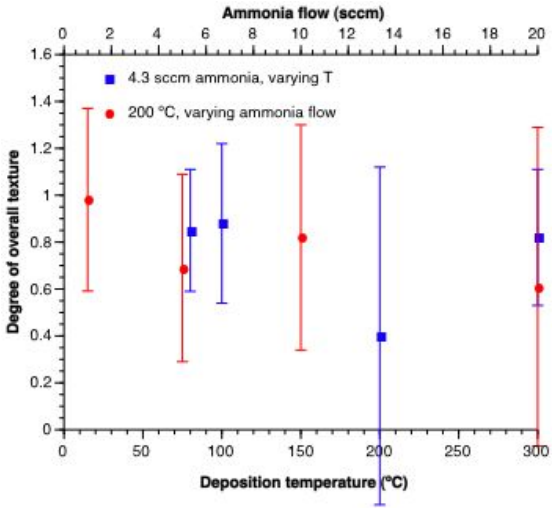

Figure 4.5: Overall degrees of texture (σ) for films grown from **2** and ammonia.

different nanometer-sized areas of the film, all exhibit diffraction spots from one or several crystalline grains (Figure 4.9). The grain sizes calculated directly from the diffraction patterns are the same as those calculated from the Scherrer equation and the XRD data, within the margin of error.

Auger electron spectroscopy (AES) suggests that the Mn : N ratio within the deposited films is essentially independent of flux and temperature and is roughly 2 : 1; i.e., somewhat depleted in nitrogen compared with the 1.5 : 1 ratio expected from the XRD results (figure 4.11, figure 4.10). For example, the AES spectra of films grown at < 200 °C and an ammonia flux of 4.3 sccm show that the composition is approximately 70% Mn and 30% N. Below 200 °C, the carbon content is below the detection limit (< 1 atomic %), but at 300 °C the films contain nearly equal amounts nitrogen and carbon, with the Mn : N : C ratio being approximately 4 : 1 : 1 (figure 4.10). This result is consistent with the XRD results, which show the presence of $Mn_{23}C_6$ at these higher temperatures.

Very similar compositions are deduced from X–ray photoelectron spectroscopy (XPS). For example, films grown at 200 °C and at ammonia fluxes between 1 and 20 sccm consist on average of 75% Mn and 25% N (figure 4.11). The N 1*s* XPS binding energies are consistent with the presence of nitride.

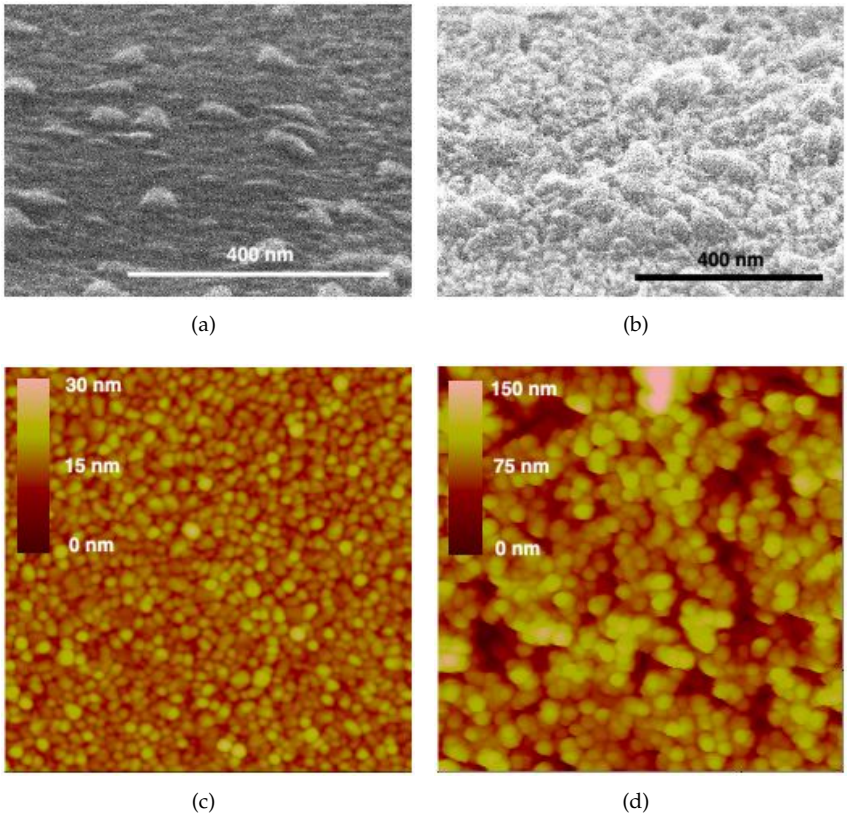

Figure 4.6: Effect of annealing on microstructure and roughness. a) and c) show SEM and AFM micrographs of a 95 nm η–Mn_3N_2 film grown at 200 °C and 5 sccm ammonia flow, as deposited. The RMS roughness is 2.30 nm. b) and d) show SEM and AFM micrographs of a 119 nm thick η–Mn_3N_2 film grown at 200 °C and 5 sccm ammonia flow, annealed at 500 °C for two hours. The RMS roughness is 21.04 nm.

Because no crystalline manganese is detected by either XRD or TEM, the $\sim$2 : 1 to $\sim$3 : 1 Mn : N ratio most likely is due to understoichiometric incorporation of nitrogen into the films, so that the phase present is best represented as η–Mn_3N_2, $0.5 < x < 1$.

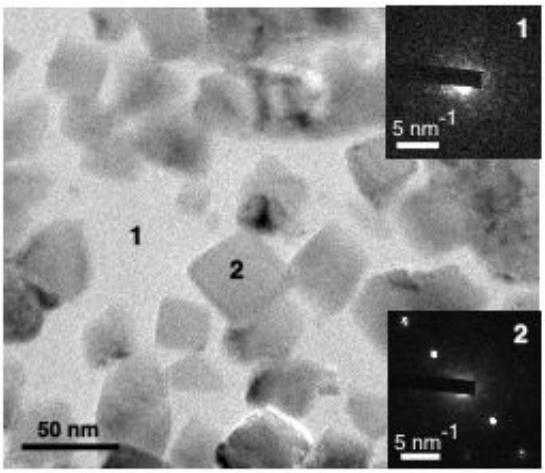

Figure 4.7: Brightfield transmission electron micrograph of 50 nm Mn_3N_2 film grown from **2** at 100 °C and 5 sccm of ammonia. Insets: Nanodiffraction patterns from areas 1 and 2 indicated in brightfield micrograph.

4.3.2 Roughness and microstructure

The smoothest films, with a root–mean–square (RMS) roughness of 1.9 nm, are obtained at 200 °C and an ammonia flux of 10 sccm. These films also have the lowest relative roughness (ratio of roughness to average thickness) of 1.6%. The roughest films, with a RMS roughness of 12 nm, are the mixed–phase films grown at 300 °C with an ammonia flux of 4.3 sccm. Films grown at 80 °C and an NH_3 flow of 4.3 sccm have a roughness 8.6 nm, but have the highest relative roughness of 12%.

Scanning electron microscopy (SEM) shows that the films grown at 80 and 100 °C at an ammonia flux of 4.3 sccm consist of very well–defined and separated columns (Figure 4.13 a). Such columnar microstructures are often observed in films grown by physical vapor deposition techniques[31] or by CVD when the sticking coefficient of the precursor is high and surface mobility is low.[147] At 200 °C the columns are clearly visible, but touch to form a more compact microstructure (Figure 4.13 b). At this temperature, the microstructure is independent of the ammonia flux between 1 and 10 sccm. The mixed-phase film deposited at 300 °C exhibits a rod–like microstructure (Figure 4.13 c), also

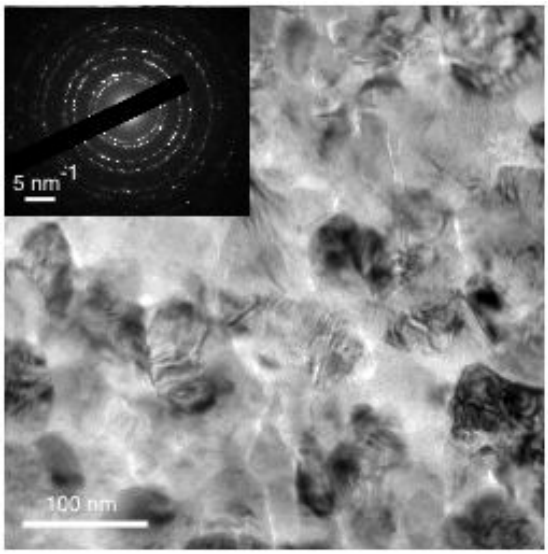

Figure 4.8: Brightfield transmission electron micrograph of a 190 nm thick η–Mn_3N_2 film grown from **2** at 200 °C and 5 sccmof ammonia. Inset shows a typical multigrain diffraction pattern from the film, indicating polycrystalline η–Mn_3N_2.

visible in atomic force microscopy scans (Figure 4.12).

4.3.3 Growth rate and temperature

The growth rate depends on the fluxes of ammonia and precursor. For a fixed precursor flux, a plot of growth rate at 200 °C versus ammonia flux shows a flux–limited regime between $1-5$ sccm, and a reaction–limited regime between 5 and 20 sccm (figure 4.15). In the flux–limited regime, the growth rate increases from 2.4 nm/min to 5.3 nm/min for the fluxes examined. The relationship is approximately linear with a slope of 0.75 (i.e., doubling the ammonia flux increases the growth rate by a factor of 1.5). The growth rate in the reaction–limited regime at 200 °C is 5.6 ± 0.7 nm/min.

At an ammonia flux of 40 sccm, the growth rate is near zero, indicating that a second flux–dependent regime is established somewhere between 20 and 40 sccm. One possible cause of this behavior is that the large ammonia

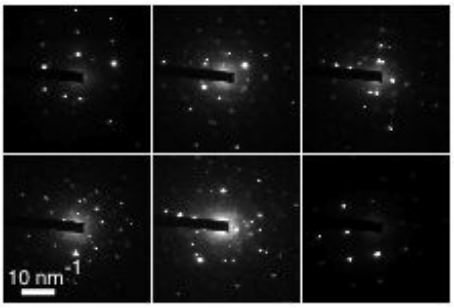

Figure 4.9: Nanodiffraction patterns from 190 nm η–Mn_3N_2 film grown from **2** at 200 °C and a flux of 5 sccm ammonia. Each pattern is taken from a different nanometer-sized point of the film. All of the diffraction patterns show clear crystalline diffraction spots from one or several grains of η–Mn_3N_2.

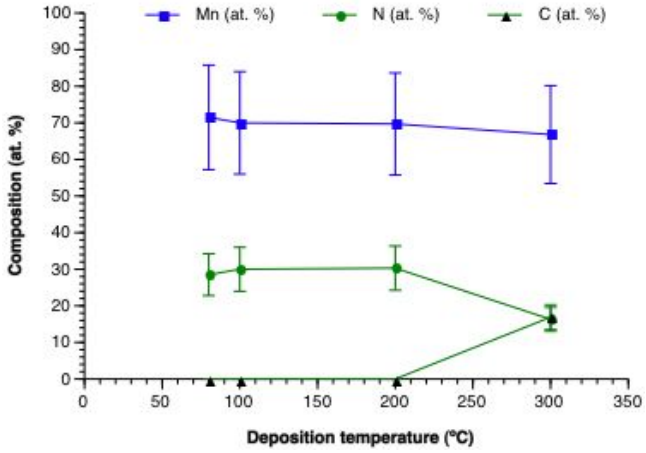

Figure 4.10: AES–derived composition of films grown from **2** and 4.3 sccm of ammonia as a function of temperature.

fluxes could block surface reactive sites, preventing the precursor from adsorbing and reacting on the surface. Ammonia is known to have a high sticking coefficient, especially at low temperatures.[150] For TiN deposition, alternately adsorbed monolayers of TDAT and ammonia do not react with one another under ultrahigh vacuum conditions, despite the low activation energy of the reaction[148]; in some way, the surface prevents attack of ammonia on the tita-

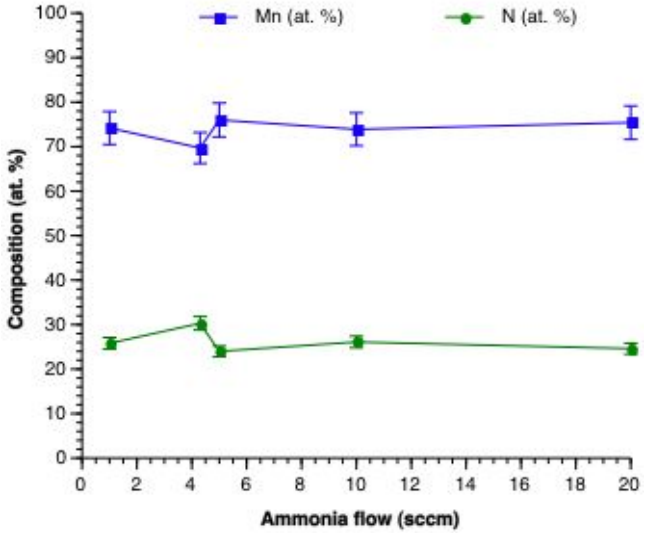

Figure 4.11: XPS–derived composition of films grown from **2** at 200 °C as a function of ammonia flux.

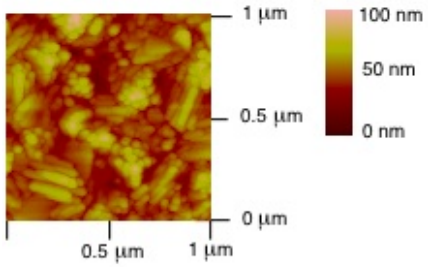

Figure 4.12: Atomic force micrograph of the roughness of a mixed–phase manganese nitride film grown from **2** at 300 °C and 4.3 sccm of ammonia.

nium center.[139] If similar phenomena govern the reaction of **2** and ammonia, an adlayer of ammonia may effectively passivate the surface. An alternative explanation of the zero growth rate at high ammonia fluxes is that ammonia may react with the precursor in the gas phase and prevent the precursor from reaching the substrate. Although we have not investigated the gas–phase reactions of **2** and NH_3, near room–temperature gas–phase reactions dominate the

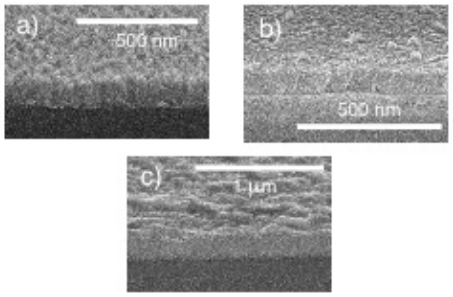

Figure 4.13: Scanning electron micrographs of manganese nitride films grown from **2** and 4.3 sccm of ammonia. a) 89 nm thick film of η–Mn_3N_2, grown at 80 °C. b) 73 nm thick film of η–Mn_3N_2, grown at 200 °C. c) 185 nm thick mixed-phase film of η–Mn_3N_2, ξ-phase $Mn_2N_{1.08}$, and cubic $Mn_{23}C_6$, grown at 300 °C.

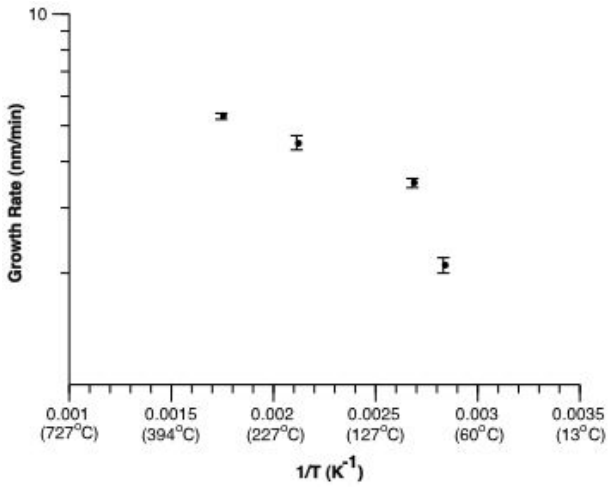

Figure 4.14: Arrhenius plot of η–Mn_3N_2 films grown from **2** at a constant flux of 4.3 sccm ammonia.

deposition of TiN from TDAT and NH_3.

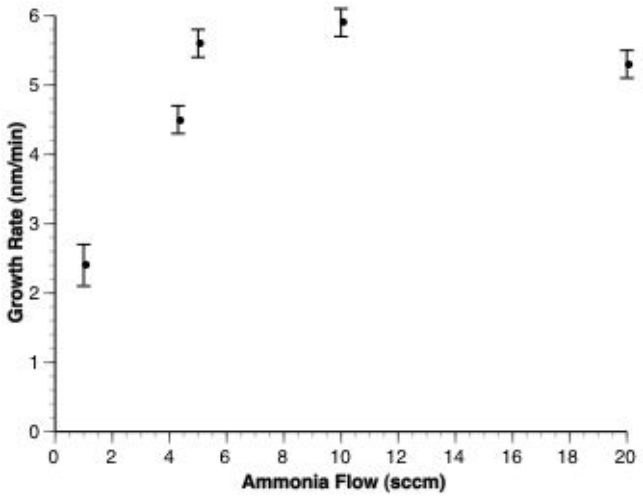

Figure 4.15: Growth rate vs. ammonia flux for η–Mn_3N_2 films grown from **2** at 200 °C. The average growth rate between 5 and 20 sccm ammonia flux is 5.6 ± 0.7 nm/min. Film growth at an ammonia flux of 40 sccm was near zero.

4.3.4 Film deposition in the absence of ammonia

Deposition from **2** in the absence of ammonia requires higher growth temperatures (300–500 °C) and the resulting films are of poor quality. AES gives carbon contents of 15–42%, Mn contents of 5–20%, and O contents of 38–70%; the latter is due to oxidation of the films in air. Nitrogen is not present in detectable amounts. This behavior is similar to the chemistry seen for other transition metal amides. For example, the titanium precursor TDAT deposits a mixed titanium carbide/nitride.[139, 151] Peaks due to elemental manganese can be seen in some of the XRD diffractograms of the material deposited from **2**. Similarly, transition metal complexes of the bis(trimethylsilyl)amido ligand, which is the silicon analog of the di(*tert*–butyl)amido group, have also been shown to react with ammonia[152] but give elemental metals (sometimes contaminated with carbon) when used as CVD precursors in the absence of ammonia.[143]

4.3.5 The mechanism of manganese nitride deposition

Our results strongly suggest that deposition of η–Mn_3N_2 from **2** and ammonia involves a transamination reaction in which Mn–N(*t*–Bu_2) ligands react with ammonia to give M–NH_2 groups and di(*tert*–butyl)amine, which then leaves the growth surface. Subsequent hydrogen transfer reactions generate η–Mn_3N_2. Note that the formal oxidation state of this material is +2, which is the same as in the precursor bis[di(*tert*)–butyl)amido]manganese(II). This mechanism operates in metal nitride depositions from other metal amide precursors. In the absence of ammonia, γ–hydrogen elimination reactions involving the di(*tert*–butyl)amide ligand most likely generate a metallacycle containing a Mn–C bond, which then causes incorporation of carbon into the film. This hypothesis is indirectly supported by the finding that carbon in the films deposited at 300 °C is present as manganese carbide rather than a carbon phase. It is possible that manganese nitride films free of carbon could be obtained at 300 °C by using higher ammonia fluxes than we examined, so that the rate of the transamination reaction exceeds the rate of γ–hydrogen elimination from the di(*tert*–butyl)amido ligands.

Two aspects of the reaction of **2** with ammonia to give η–Mn_3N_2 are notable. First, the deposition can be carried out to give pure films at the remarkably low temperature of 80 °C. Second, the films obtained at this temperature are crystalline. Both of these aspects may reflect special aspects of the electronic structure of the metal center. The manganese atom in **2** is in the +2 oxidation state, and the five *d*–electrons adopt a high–spin electronic configuration with five unpaired electrons.[153] Complexes with high–spin transition metal centers are often kinetically labile, meaning that they undergo ligand substitution reactions very rapidly.[154] The high–spin Mn^{II} center in **2** is likely to remain high–spin, and therefore labile, throughout a significant fraction of the reaction sequence that leads to film growth. As a result, reactive surface species remain mobile on the surface throughout much of the reaction pathway leading to nitride growth, and can settle into low–energy ordered arrangements before they become incorporated into the bulk by subsequent deposition activity. The crystallinity and rapid growth rates can therefore attributed to the labile metal–ligand bonding characteristic of high–spin Mn^{II}.

CHAPTER 5

Conclusions

In this dissertation, two new chemical vapor deposition processes are detailed. The first is a conformal process for deposition of metallic ruthenium for use in interconnects and DRAM electrodes. The second is the first chemical vapor deposition process for any phase of manganese nitride, in this case mainly η–Mn_3N_2, for use as active magnetic layers or as a dopant for GaN for spintronics.

5.1 Low-temperature chemical vapor deposition of ruthenium

The ruthenium process is based on thermolysis of the precursor **1**. The reaction is likely $(C_6H_8)Ru(CO)_3 \rightarrow Ru + C_6H_6 + H_2 + 3\,CO$ and is facile with an activation energy of only 18 kJ/mol, but the growing ruthenium film catalyzes the dissociation of the benzene into bound surface fragments that result in ∼30 atomic percent carbon and trace hydrogen incorporation.

Thin crystalline ruthenium films can be deposited from tricarbonyl(1,3–cyclohexadiene)ruthenium(0) in the temperature range 150 to 500 °C onto chromium, bare silicon(1 0 0), silicon dioxide, and *c*-plane sapphire substrates in the absence of a carrier gas. The nucleation delays generally ranged from a few seconds to a few minutes. The process is very conformal and is projected to coat a via with an aspect ratio of 20 : 1 with over 90 % conformality. The conformality is likely due to siteblocking of the growing film surface at precursor partial pressures above 2 mTorr and the low sticking coefficient of tricarbonyl(1,3–cyclohexadiene)ruthenium(0).

The growth rates ranged between 2 and 24 nm/min, significantly higher than most previous processes. The microstructures are compact zone T microstructures with no visible column boundaries or facets, in part because the film growth proceeds through repeated renucleation. In Ru films grown on insulating substrates, the resistivities decrease from 219 μΩ·cm to 24 μΩ·cm with increasing grain sizes from ∼20 nm to ∼200 nm. The larger grain sizes often required growth temperatures of over 400 °C. The increase in resistivity above bulk value (7.2 μΩ·cm) can be attributed to grain boundary scattering and impurity scattering.

On all substrates, the ruthenium films exhibited clear overall texture at temperatures below 350 °C, which disappeared as the deposition temperatures were raised. Despite the different surface crystallographies of the substrates, the role of the substrate in creating the texture was very small, even on an epitaxial substrate. The textures form during film thickening and can be explained by kinetically driven alignment of the highest–energy plane parallel to the surface below homologous temperatures of approximately 0.2 and by kinetically driven dominance of grains with orientations that result in the fastest lateral grain growth at temperatures above that.

5.2 Low-temperature chemical vapor deposition of manganese nitride

The manganese nitride process is based on the very facile reaction of bis[di(*tert*)–butyl)amido]manganese(II) with ammonia. Specular, bronze-colored crystalline thin films can be deposited at temperatures as low as 80 °C. The growth rates range from 2.4 to 5.6 nm/min. The crystallinity and for the deposition temperatures rapid growth rates can be attributed to the labile metal–ligand bonding characteristic of high–spin Mn^{II}.

At 80 °C and 100 °C, the films consist of a ∼23 % volume fraction of tetragonal η–Mn_3N_{2-x}, where $0.5 < x < 1$, crystallites embedded in a amorphous matrix. At 200 °C, the η–Mn_3N_{2-x} films were nearly completely crystalline. At 300 °C, the films consist of 40 atomic percent $Mn_2N_{1.08}$, 40 atomic percent Mn_3N_2, and 20 atomic percent $Mn_{23}C_6$. The sticking coefficient of bis[di(*tert*)–

butyl)amido]manganese(II) is high, which results in columnar microstructures in the η–Mn_3N_2 films, although the mixed-phase film grown at 300 °C has a compact, rod–like microstructure. At 200 °C, the process transitions from flux–limited to reaction–limited at 5 sccm ammonia flow. The films exhibit significant (1 1 0) texture, which is consistent with kinetically driven dominance of grains with orientations that result in the fastest lateral grain growth.

The reaction between bis[di(*tert*)–butyl)amido]manganese(II) and ammonia involves a transamination reaction in which Mn–N(*t*–Bu)$_2$ ligands react with ammonia to give M–NH_2 groups and di(*tert*–butyl)amine. Subsequent hydrogen transfer reactions generate nitrogen–deficient η–Mn_3N_2. In the absence of ammonia, γ–hydrogen elimination reactions involving the di(*tert*–butyl)amine ligand in Mn[N(*t*–Bu)$_2$]$_2$ most likely generate a metallocycle containing a Mn–C bond, which then causes carbon incorporation into the film.

References

[1] Giblin, R. *Phys. Ed.* **1979**, *14*, 406–410.

[2] Streetman, B. G.; Banerjee, S. *Solid State Electronic Devices*; Prentice Hall: Upper Saddle River, NJ.

[3] Shockley, W.; Hooper, W. W.; Quelsser, H. J.; Schroen, W. *Surf. Sci. Science* **1964**, *2*, 277–287.

[4] Chang, M. H.; Zhang, J. F.; Zhang, W. D. *IEEE T. Electron. Dev.* **2006**, *53*, 1347–1354.

[5] Zhang, W. D.; Zhang, J. F.; Lalor, A.; Burton, D.; Groeseneken, G. V.; Degraeve, R. *IEEE T. Electron. Dev.* **2002**, *49*, 1868–1875.

[6] Gnadinger, F. P.; Huebner, G. G.; Derbenwick, G. F.; Devilbiss, A. D. *Ferroelectrics* **2002**, *268*, 729–734.

[7] Kaloyeros, A. E.; Eisenbraun, E. *Annu. Rev. Mater. Sci.* **2000**, *30*, 363–385.

[8] Hartfield, C. D.; Ogawa, E. T.; Park, Y.-J.; Chiu, T.-C.; Guo, H. *IEEE Trans. Dev. Mat. Rel.* **2004**, *4*, 129–141.

[9] Rafaja, D.; Schimpf, C.; Klemm, V.; Schreiber, G.; Bakonyi, I.; Peter, L. *Acta Mater.* **2009**, *57*, 3211–3222.

[10] Liu, J.; Liu, C.; Conway, P. P. author, 2008; pp 679–684.

[11] Bardeen, J.; Brattain, W. H. *Phys. Rev.* **1949**, *75*, 1208.

[12] Kilby, J. S.; Keonjian, E. *Techn. Dig. IEDM* **1959**, *5*, 76.

[13] Kilby, J. S. *IEEE T. Electron. Dev.* **1976**, *23*, 648.

[14] Datamonitor, *Global Semiconductors Industry Profile*, 0199-0682, December 2008.

[15] Friedman, T. L. *The Lexus and the Olive Tree*; Anchor Books: New York, NY, 2000.

[16] Friedman, T. L. *The World Is Flat*; Farrar, Straus and Giroux: New York, NY, 2005.

[17] Appadurai, A. *Modernity at Large: Cultural Dimensions of Globalization*; University of Minnesota Press: Minneapolis, MN, 1949.

[18] Rosenau, J. N. *Distant Proximities: Dynamics Beyond Globalization*; Princeton University Press: Princeton, NJ, 2003.

[19] *The Globalization Reader*; Lechner, F.; Boli, J., Eds.; Blackwell Publishers: Malden, MA, 2000.

[20] Margolis, J.; Fisher, A. *Unlocking the Clubhouse: Women in Computing*; MIT Press: Cambridge, MA, 2003.

[21] Oudshoorn, N.; Pinch, T. *How Users Matter*; MIT Press: Cambridge, MA, 2005.

[22] Hu, C. K.; Harper, J. M. E. *Mat. Chem. Phys.* **1998**, *52*, 5–16.

[23] Frank, M. M.; Kim, S.-B.; Brown, S. L.; Bruley, J.; Copel, M.; Hopstaken, M.; Chudzik, M.; Narayanan, V. *Microelectron. Eng.* **2009**, *86*, 1603–1608.

[24] *A Thorough Examination of the Electronic Chemicals and Materials Markets*; Businesswire, August 15, 2007.

[25] Lee, M. L.; Fitzgerald, E. A.; Bulsara, M. T.; Currie, M. T.; Lochtefeld, A. *J. Appl. Phys.* **2005**, *97*, 011101.

[26] Ezhilvalavan, S.; Tseng, T.-Y. *Mat. Chem. Phys.* **2000**, *65*, 227–248.

[27] Scott, J. F. *Annu. Rev. Mater. Sci.* **1998**, *28*, 79–100.

[28] Thompson, S. E.; Pathasarathy, S. *Materials Today* **2006**, *9*, 20–25.

[29] *The International Technology Roadmap for Semiconductors 2007 Edition*, Semicond. ind. assoc. technical report, 2007.

[30] Ferrer, J.; García-Suárez, V. M. *J. Mat. Chem.* **2009**, *19*, 1696–1717.

[31] Ohring, M. *Materials Science of Thin Films*; Academic Press: San Diego, CA, 2002.

[32] Aaltonen, T.; Alén, P.; Ritala, M.; Leskelä, M. *Chem. Vap. Dep.* **2003**, *9*, 45–49.

[33] Leskelä, M.; Ritala, M. *Thin Solid Films* **2002**, *409*, 138–146.

[34] Wulu, H. C.; Saraswat, K. C.; Mcvittie, J. P. *J. Electrochem. Soc.* **1991**, *138*, 1831.

[35] Nuruddin, A.; Doyle, J.; Abelson, J. *J. Appl. Phys.* **1994**, *76*, 3123–3129.

[36] Jayaraman, S.; Yang, Y.; Kim, D. Y.; Girolami, G. S.; Abelson, J. R. *J. Vac. Sci. Tech. A* **2005**, *26*, 1619–1625.

[37] Aoyama, T.; Eguchi, K. *Jpn. J. Appl. Phys.* **1999**, *38*, 1134–1136.

[38] Iizuka, T.; Arita, K.; Yamamoto, I.; Yamamichi, S. *NEC Res. Dev.* **2001**, *42*, 64–9.

[39] Yamamichi, S. et al. *IEEE T. Electron. Dev.* **1997**, *44*, 1076–1083.

[40] Bandaru, J.; Sands, T.; Tsakalakos, L. *J. Appl. Phys.* **1998**, *84*, 1121–1125.

[41] Maiwa, H.; Ichinose, N.; Okazaki, K. *Jpn. J. Appl. Phys.* **1994**, *33*, 5223–5226.

[42] Wei, P.; Desu, S. *Phys. Stat. Sol. (a)* **1997**, *161*, 201–215.

[43] Lesaicherre, P. Y.; Yamamichi, S.; Takemura, K.; Yamaguchi, H.; Tokashiki, K.; Miyasaka, Y.; Yoshida, M.; Ono, H. *Integr. Ferroelectr.* **1995**, *11*, 81–100.

[44] Pan, W.; Desu, S. B. *J. Vac. Sci. Tech. B* **1994**, *12*, 3208–3213.

[45] Vijay, D. P.; Desu, S. B.; Pan, W. *J. Electrochem. Soc.* **1993**, *140*, 2635–2639.

[46] Saito, S.; Kuramasu, K. *Jpn. J. Appl. Phys.* **1992**, *31*, 135–138.

[47] Misra, V.; Lucovsky, G.; Parsons, G. *MRS Bull.* **2002**, *27*, 212–216.

[48] Michaelson, H. B. *J. Appl. Phys.* **1977**, *48*, 4729–4733.

[49] Zhong, H.; Heuss, G.; Misra, V. *IEEE Electron Dev. Lett.* **2000**, *21*, 593–595.

[50] Chan, R.; Arunagiri, T.; Zhang, Y.; Chyan, O.; Wallace, R. M.; Kim, M. J.; Hurd, T. Q. *Electrochem. Solid-State Lett.* **2004**, *7*, G154–G157.

[51] Cho, S. K.; Kim, S.-K.; Kim, J. J.; Oh, S. M. *J. Vac. Sci. Tech. B* **2004**, *22*, 2649–2653.

[52] Chyan, O.; Arunagiri, T. N.; Ponnuswamy, T. *J. Electrochem. Soc.* **2003**, *150*, C347–C350.

[53] Kwon, O.-K.; Kim, J.-H.; Park, H.-S.; Kang, S.-W. *J. Electrochem. Soc.* **2004**, *151*, G109–G112.

[54] Kwon, O.-K.; Kwon, S.-H.; Park, H.-S.; Kang, S.-W. *J. Electrochem. Soc.* **2004**, *151*, C753–C756.

[55] Moffat, T. P.; Walker, M.; Chen, P. J.; Bonevich, J. E.; Egelhoff, W. F.; Richter, L.; Witt, C.; Aaltonen, T.; Ritala, M.; Leskelä, M.; Josella, D. *J. Electrochem. Soc.* **2006**, *153*, C37–C50.

[56] Trent, D. E.; Paris, B.; Krause, H. H. *Inorg. Chem.* **1964**, *3*, 1057–1058.

[57] Park, S. E.; Kim, H. M.; Kim, K. B.; Min, S. H. *J. Electrochem. Soc.* **2000**, *147*, 203–209.

[58] Kang, S. Y.; Choi, K. H.; Lee, S. K.; Hwang, C. S.; Kim, H. J. *J. Electrochem. Soc.* **2000**, *147*, 1161–1167.

[59] Matsui, Y.; Hiratani, M.; Nabatame, T.; Shimamoto, Y.; Kimura, S. *Electrochem. Solid-State Lett.* **2002**, *5*, C18–C21.

[60] Nabatame, T.; Hiratani, M.; Kadoshima, M.; Shimamoto, Y.; Matsui, Y.; Ohji, Y.; Asano, I.; Fujiwara, T.; Suzuki, T. *Jpn. J. Appl. Phys.* **2000**, *39*, 1188–1190.

[61] Kadoshima, M.; Nabatame, T.; Hiratani, M.; Nakamura, Y.; Asano, I.; Suzuki, T. *Jpn. J. Appl. Phys.* **2002**, *41 part 2*, L347–L350.

[62] Lai, Y.-H.; Chen, Y.-L.; Chi, Y.; Liu, C.-S.; Carty, A. J.; Peng, S.-M.; Lee, G.-H. *J. Mat. Chem.* **2003**, *13*, 1999–2006.

[63] Lee, J.-H.; Kim, J.-Y.; Rhee, S.-W.; Yang, D.; Kim, D.-H.; Yang, C.-H.; Han, Y.-K.; Hwang, C.-J. *J. Vac. Sci. Tech. A* **2000**, *18*, 2400–2403.

[64] Kang, S. Y.; Lim, H. J.; Hwang, C. S.; Kim, H. J. *J. Electrochem. Soc.* **2002**, *149*, C317–C323.

[65] Kang, S. Y.; Hwang, C. S.; Kim, H. J. *J. Electrochem. Soc.* **2005**, *152*, C15–C19.

[66] Green, M. L.; Gross, M. E.; Papa, L. E.; Schnoes, K. J.; Brasen, D. *J. Electrochem. Soc.* **1985**, 2677.

[67] Wang, Q.; Ekerdt, J. G.; Gay, D.; Sun, Y.-M.; White, J. M. *Appl. Phys. Lett.* **2004**, *84*, 1380–1382.

[68] Schneider, A.; Popovska, N.; Holzmann, F.; Gerhard, H.; Topf, C.; Zenneck, U. *Chem. Vap. Dep.* **2005**, *11*, 99–105.

[69] Schneider, A.; Popovska, N.; Jipa, I.; Atakan, B.; Siddiqi, M. A.; Siddiqui, R.; Zenneck, U. *Chem. Vap. Dep.* **2007**, *13*, 389–395.

[70] Choi, J.; Choi, Y.; Hong, J.; Tian, H.; Roh, J.-S.; Kim, Y.; Chung, T.-M.; Woo Oh, Y.; Kim, Y.; Kim, C. G.; No, K. *Jpn. J. Appl. Phys.* **2002**, *41*, 6852–6856.

[71] Gatineau, J.; Dussarrat, C. *Surf. Coat. Tech.* **2007**, 9146–9148.

[72] Jakob, P.; Menzel, D. *Surf. Sci.* **1988**, *210*, 503–530.

[73] Jakob, P. *Doctoral dissertation*, Technische Universität München, 1989.

[74] Heimann, P. A.; Jakob, P.; Pache, T.; Steinrück, H.-P.; Menzel, D. *Surf. Sci.* **1989**, *210*, 282–300.

[75] Payne, S.; McEwen, J.-S.; Kreuzer, H.; Menzel, D. *Surf. Sci.* **2005**, *594*, 240–262.

[76] Pfnür, H.; Menzel, D. *Journal of Chemical Physics* **1983**, *79*, 2400–2410.

[77] Schneider, A. *Doctoral dissertation*, Universität Erlangen-Nürnberg, 2006.

[78] Manner, W. L.; Girolami, G. S.; Nuzzo, R. G. *J. Phys. Chem. B* **1998**, *102*, 10295–10306.

[79] Hammer, B.; Nørskov, J. K. In *Theoretical surface science and catalysis–calculations and concepts Advances in Catalysis*; Gates, B. C.; Knözinger, H., Eds.; Academic Press, 2000; Vol. 45, pp 71–129.

[80] Uhlenbrock, S.; Vaartstra, B. A. *Methods for preparing ruthenium and osmium compounds, US Patent 372427*, 2000.

[81] Lienhard, M. A.; Hoover, C. A. *Methods of synthesizing ruthenium and osmium complexes, US patent 963452*, 2002.

[82] Jeffries, P. M.; Dubois, L. H.; Girolami, G. S. *Chem. Mat.* **1992**, *4*, 1169–1175.

[83] Ma, C.-H.; Huang, J.-H.; Chen, H. *Thin Solid Films* **2002**, 73–78.

[84] Yamada, S.; Nishibe, Y.; Saizaki, M.; Kitajima, H.; Ohtsubo, S.; Morimoto, A.; Shimizu, T.; Ishida, K.; Masaki, Y. *Jpn. J. Appl. Phys.* **2002**, *41*, L206–L208.

[85] Lim, B. S.; Rahtu, A.; Gordon, R. G. *Nat. Mater.* **2003**, *2*, 749–754.

[86] *CRC Handbook of Chemistry and Physics*; 82nd ed.; CRC Press: Boca Raton, FL, 2001.

[87] Rossnagel, S. M.; Kuan, T. S. *J. Vac. Sci. Tech. B* **2004**, *22*, 240–247.

[88] Mola,; Heras, *Electrocomp. Sci. Tech.* **1974**, *1*, 77.

[89] Kuan, T. S.; Inoki, C. K.; Oehrlein, G. S.; Rose, K.; Zhao, Y.-P.; Wang, G.-C.; Rossnagel, S. M.; Cabral, C. Materials Research Society Proceedings Spring 2000, San Fransisco, 2000.

[90] Mayadas, A. F.; Shatzkes, M. *Phys. Rev. B* **1970**, *1*, 1382.

[91] Khan, M. S. R. *Physica Status Solidi (a)* **1986**, *96*, 651–655.

[92] Angadi, M. A. *J. Mat. Sci.* **1985**, *20*, 761–796.

[93] Tellier, C. R. *J. Mat. Sci.* **1985**, *20*, 1901–1919.

[94] Davis, L. E.; MacDonald, N. C.; Palmberg, P. W.; Riach, G. E.; Weber, R. E. *Handbook of Auger Electron Spectroscopy*; Physical Electronics Division, Perkin-Elmer Corporation: Eden Prairie, Minnesota, 1976.

[95] Moulder, J.; Stickle, W. F.; Sobol, P. E.; Bomben, K. D. *Handbook of X-ray Photoelectron Spectroscopy*; Physical Electronics Division, Perkin-Elmer Corporation: Eden Prairie, Minnesota, 1992.

[96] Jakob, P. *J. Chem. Phys.* **1998**, *108*, 5035–5043.

[97] Masel, R. I. *Principles of Adsorption and Reaction on Solid Surfaces*; Wiley Series on Chemical Engineering; John Wiley and Sons: New York, 1996.

[98] Pearson, R. G. *J. Am. Chem. Soc.* **1963**, *85*, 3533–3539.

[99] Hu, D. Q.; MacPherson, C. D.; Leung, K. T. *Surf. Sci.* **1992**, *273*, 21–30.

[100] Seelmann-Eggebert, M.; Zimmermann, H.; Obloh, H. MRS Spring 1997 Meeting Proceedings: Gallium Nitride and Related Materials II, Pittsburgh, PA, 1997.

[101] Gautier, M.; Durand, J. P.; Pham Van, L.; Guittet, M. J. *Surf. Sci.* **1991**, *250*, 71.

[102] Yang, Y.; Jayaraman, S.; Kim, D. Y.; Girolami, G. S.; Abelson, J. R. *Chem. Mat.* **2006**, 5088–5096.

[103] Dorgelo, A.; Vroemen, J.; Wolters, R. *Microelectron. Eng.* **2001**, *55*, 337–340.

[104] Ryu, C.; Loke, A. L. S.; Nogami, T.; Wong, S. the International Reliability Physics Symposium Proceedings, New York, NY, 1997.

[105] Kim, H.; Koseki, T.; Ohba, T.; Ohta, T.; Kojima, Y.; Sato, H.; Yoshii, N.; Shimogaki, Y. *Advanced Metallization Conference (AMC)* **2006**, *2006*, 525–530.

[106] Barrett, C. S. *The Structure of Metals*; McGraw-Hill: New York, NY, 1952.

[107] Ma, C.-H.; Huang, J.-H.; Chen, H. *Thin Solid Films* **2004**, *446*, 184–193.

[108] Licausi, N.; Yuan, W.; Tang, F.; Parker, T.; Li, H.; Wang, G.-C.; Lu, T.-M.; Bhat, I. *J. Electr. Mat.* **2009**, *38*, 1600–1604.

[109] Reimer, L.; Freking, K. *Z. Phys.* **1965**, *184*, 119–129.

[110] Bauer, E. *Z. Kristallogr.* **1956**, *107*, 72–98.

[111] Walton, D. *Phil. Mag.* **1962**, 1671.

[112] van der Drift, A. *Philips Res. Rep.* **1967**, *22*, 267–288.

[113] Machlin, E. S. *Materials Science in Microelectronics I*; Elsevier: New York, 2005.

[114] Lee, D. N. *J. Mat. Sci.* **1989**, *24*, 4375–4378.

[115] Lee, D. N. *J. Mat. Sci.* **1999**, *34*, 2575–2582.

[116] Petrov, I.; Barna, P. B.; Hultman, L.; Greene, J. E. *J. Vac. Sci. Tech. A* **2003**, *21*, S117–S128.

[117] Thompson, C. V.; Carel, R. *Mat. Sci. Eng.* **1995**, *B32*, 211–219.

[118] van der Put, P. J. *The Inorganic Chemistry of Materials*; Plenum Press: New York and London, 1998.

[119] Tian, H.-Y.; Wang, Y.; Chan, H. L.-W.; Choy, C.-L.; No, K.-S. *Journal of Alloys and Compounds* **2005**, *392*, 231–236.

[120] Wang, D.-D.; Zhang, J.-M.; Xu, K.-W. *Surf. Sci.* **2006**, *600*, 2990–2996.

[121] Glansdorff, P.; Prigogine, I. *Thermodynamic Theory of Structure, Stability and Fluctuations*; Wiley Interscience: New York, 1977.

[122] Thornton, J. A. *J. Vac. Sci. Tech. A* **1986**, *4*, 3059–3065.

[123] Kim, K. H.; Chun, J. S. *Thin Solid Films* **1986**, *141*, 287.

[124] Barrett, C. S.; Massalski, T. B. *Structure of Metals: Crystallographic Methods, Principles and Data*, 3rd ed.; McGraw-Hill: NY, 1966.

[125] Borsa, D. M.; Grachev, S.; Boerma, D. O.; Kerssemakers, J. W. *Appl. Phys. Lett.* **2001**, 994–996.

[126] Gokcen, N. A. *Bull. All. Phase Diagrams* **1990**, *11*, year.

[127] Nakagawa, S.; Naoe, M. *J. Appl. Phys.* **1994**, *75*, year.

[128] Kreiner, G.; Jacobs, H. *J. Alloys Comp.* **1992**, *183*, 345–362.

[129] Suzuki, K.; Kaneko, T.; Yoshida, H.; Obi, Y.; Fujimori, H.; Morita, H. *J. Alloys Comp.* **2000**, *306*, 66–71.

[130] Jacobs, H.; Stüve, C. *J. Less-Common Met.* **1984**, 323–329.

[131] Kane, M. H.; Asghar, A.; Vestal, C. R.; Strassburg, M.; Senawiratne, J.; Zhang, Z. J.; Dietz, N.; Summers, C. J.; Ferguson, I. T. *Semicond. Sci. Tech.* **2005**, *20*, L5–L9.

[132] Dietl, T.; Ohno, H.; Matsukura, F.; Cibert, J.; Ferrand, D. *Science* **2000**, *287*, 1019.

[133] Hu, Z. G.; Weerasekara, A. B.; Dietz, N.; Perera, A. G. U.; Strassburg, M.; Kane, M. H.; Asghar, A.; Ferguson, I. T. *Phys. Rev. B* **2007**, *75*, 205320.

[134] Yang, H.; al Brithen, H.; Smith, A. R. *Appl. Phys. Lett.* **2001**, *78*, 3860–3862.

[135] Weerasekara, A. B.; Hu, Z. G.; Dietz, N.; Perera, A. G. U.; Asghar, A.; Kane, M. H.; Strassburg, M.; Ferguson, I. T. *J. Vac. Sci. Tech. B* **2008**, *26*, 52–55.

[136] Gupta, S.; Kang, H.; Kane, M. H.; Park, E.-H.; Ferguson, I. T. *Phys. Stat. Sol. (c)* **2008**, *5*, 1740–1742.

[137] Ferguson, I. T. *Phys. Stat. Sol. (c)* **2007**, *4*, 389–396.

[138] Kurtz, S. R.; Gordon, R. G. *Thin Solid Films* **1986**, 277–290.

[139] Dubois, L. H.; Zegarski, B. R.; Girolami, G. S. *J. Electrochem. Soc.* **1992**, 3603–3609.

[140] Dubois, L. H. *Polyhedron* **1994**, *13*, 1329–1336.

[141] Prybyla, J. A.; Chiang, C. M.; Dubois, L. H. *J. Electrochem. Soc.* **1993**, 2695–2702.

[142] Fix, R. M.; Gordon, R. G.; Hoffman, D. M. *Chem. Mat.* **1990**, 235–41.

[143] Baxter, D. V.; Chisholm, M. H.; Gama, G. J.; Hector, A. L.; Parkin, I. P. *Chem. Vap. Dep.* **1995**, *1*, 49–51.

[144] Andersen, R. A.; Faegri, K., J.; Green, J. C.; Haaland, A.; Lappert, M. F.; Leung, W. P.; Rypdal, K. *Inorg. Chem.* **1988**, 1782–1786.

[145] Olmstead, M. M.; Power, P. P.; Shoner, S. C. *Inorg. Chem.* **1991**, 2547–2551.

[146] Reiff, W. M.; Schulz, C. E.; Whangbo, M.-H.; Seon, J. I.; Lee, Y. S.; Potratz, G. R.; Spicer, C. W.; Girolami, G. S. *J. Am. Chem. Soc.* **2009**, 404–405.

[147] Zhao, Y.-P.; Drotar, J. T.; Wang, G.-C.; Lu, T.-M. *Phys. Rev. Lett.* **2001**, *87*, 136102.

[148] Weiller, B. H. *J. Am. Chem. Soc.* **1996**, 4975–4983.

[149] Hillman, J. T.; Rice, M. J., J.; Studiner, D. W.; Foster, R. F.; Fiordalice, R. W. *Proc. VIMC Conf.* **1992**, 246–252.

[150] Takaoka, T.; Kusunoki, I. *Surf. Sci.* **1998**, *412/413*, 30–41.

[151] Girolami, G. S.; Jensen, J. A.; Gozum, J. E.; Pollina, D. M. *Mat. Res. Soc. Symp. Proc. 121* **1988**, 429.

[152] Baxter, D. V.; Chisholm, M. H.; Gama, G. J.; DiStasi, V. F.; Hector, A. L.; Parkin, I. P. *Chem. Mat.* **1996**, 1222–1228.

[153] Spicer, C. W. *Doctoral dissertation*, University of Illinois at Urbana-Champaign: Urbana, IL, 2008.

[154] Taube, H. *Chem. Rev.* **1952**, *50*, 69–126.

Author's Biography

Teresa Lazarz was born into a bicultural family and had lived on three continents before she turned eighteen. She is an adult third culture kid, someone who grew up in more than one culture. She received her bachelor of arts degree from Knox College in Galesburg, IL, in physics, chemistry and the equivalent of a minor in mathematics. After college, Teresa wanted to tackle the challenge of understanding what happens close to an edge in a real material, something undergraduate physics courses often leave unadressed due to its complexity, and went into interdisciplinary research on thin films.

Teresa also has a long–standing interest in business and management, which started with reading her father's management books when she was in her teens. During her time in graduate school, she worked part–time for Illinois Business Consulting, the nation's largest student–run consulting firm. Teresa started as a consultant, then got promoted to project manager and became an ISO–certified Project Management Professional (PMP) in 2008.